

MIT Open Access Articles

This is a supplemental file for an item in DSpace@MIT

Item title: Electrochemical Polarization Dependence
of the Elastic and Electrostatic Driving Forces
to Aliovalent Dopant Segregation on LaMnO₃

Link back to the item: <https://hdl.handle.net/1721.1/125825>



Electrochemical polarization dependence of the elastic and electrostatic driving forces to aliovalent dopant segregation on LaMnO_3

Dongha Kim^{*a}, Roland Bliem^{*b}, Franziska Hess^{*b}, Jean-Jacques Gallet^{c,d}, and Bilge Yildiz^{a,b}

- a Department of Materials Science and Engineering, Massachusetts Institute of Technology, 77 Massachusetts Avenue, Cambridge, MA, 02139, USA
 - b Department of Nuclear Science and Engineering, Massachusetts Institute of Technology, 77 Massachusetts Avenue, Cambridge, MA, 02139, USA
 - c Sorbonne Université, CNRS, Laboratoire de Chimie Physique Matière et Rayonnement, UMR 7614, 4 place Jussieu, 75005 Paris, France
 - d Synchrotron SOLEIL, L'Orme des Merisiers, Saint-Aubin, 91192 Gif sur Yvette, France
- E-mail of corresponding author: byildiz@mit.edu

Abstract

Segregation of aliovalent dopant cations is a common degradation pathway on perovskite oxide surfaces in energy conversion and catalysis applications. Here we focus on resolving quantitatively how dopant segregation is affected by oxygen chemical potential, which varies over a wide range in electrochemical and thermochemical energy conversion reactions. We employ electrochemical polarization to tune the oxygen chemical potential over many orders of magnitude. Altering the effective oxygen chemical potential causes the oxygen non-stoichiometry to change in the electrode. This then influences the mechanisms underlying the segregation of aliovalent dopants. These mechanisms are (i) the formation of oxygen vacancies that couples to the electrostatic energy of the dopant in the perovskite lattice, and (ii) the elastic energy of the dopant due to cation size mismatch, which also promotes the reaction of the dopant with O_2 from the gas phase. The present study resolves these two contributions over a wide range of effective oxygen pressures. Ca-, Sr-, and Ba-doped LaMnO_3 are selected as model systems, where the dopants have the same charge but different ionic sizes. We found that there is a transition between the electrostatically and elastically dominated segregation regimes, and the transition shifted to a lower oxygen

pressure with increasing cation size. This behavior is consistent with the results of our *ab-initio* thermodynamics calculations. The present study provides quantitative insights into how the elastic energy and the electrostatic energy determine the extent of segregation for a given overpotential and atmosphere relevant to the operating conditions of perovskite oxides in energy conversion applications.

1. Introduction

Perovskite oxides (ABO_3) are considered key players in clean energy conversion applications, including in solid oxide fuel cells (SOFCs) ¹⁻⁷, gas separation membranes ⁸, catalysts for gas conversion/reformation ⁹⁻¹⁴ and syngas production ¹⁵. They are also important in advanced electronics and energy storage devices, such as memristive switches ¹⁶ and batteries ¹⁷⁻¹⁸. The diffusion and charge exchange processes occurring in the bulk of such material are considered well established ¹⁹. On the other hand, understanding of surface processes is yet incomplete ²⁰⁻²⁵, despite their importance in determining the performance of the material in all the above stated applications.

In fuel and electrolysis cells ²⁶, oxygen exchange (reduction and evolution) reactions at the surface are considered a bottleneck constraining their efficiency. The activity for these reactions suffers from long-term degradation at high temperatures from 700°C to 1000°C, oxidizing atmospheres ^{1, 27}, such as air or pure oxygen, and cell voltages, which can approach over 1 V. It is thus important to resolve the reasons of surface degradation under these operation conditions in order to increase the long-term efficiency of the cells. In La-based mixed conducting perovskites such as $\text{La}_{1-x}\text{Sr}_x\text{CoO}_3$ (LSC) or doped manganites $\text{La}_{1-x}\text{D}_x\text{MnO}_3$ ($\text{D} = \text{Ca}^{2+}, \text{Sr}^{2+}, \text{Ba}^{2+}$; LCM, LSM, and LBM, respectively), one of the key mechanisms behind the decrease in reactivity to oxygen exchange reactions is the segregation and precipitation of aliovalent dopant cations. The formation of an inactive surface oxide phase ²⁸⁻³³ on these materials drastically decreases the initially high activity for the oxygen reduction reaction.

One difficulty in the study of dopant segregation in doped LaMnO_3 and related compounds arises from the fact that segregation kinetics and thermodynamics cannot be easily separated. In addition, bulk and surface contributions to segregation are not independent of each other. This leads to a large number of material parameters (such as composition and microstructure) and

process parameters (such as temperature, oxygen partial pressure, and applied potential) that have been shown to influence segregation, as will be summarized in the following short overview.

As for modifying the composition, adjusting the bulk A-site deficiency in perovskite oxides has been shown to reduce dopant segregation³⁴⁻³⁵. On the other hand, doping additional metal cations at the surface can change the reducibility locally. This has been shown to modify the intensity of segregation by altering the surface oxygen vacancy concentration³⁶. These two examples highlight that both bulk and surface can play a role in dopant segregation through changes in the defect concentrations, either locally at the surface or in the bulk. From the bulk perspective, the sample microstructure and the presence of extended defects in a film, such as grain boundaries or dislocations can also facilitate segregation³⁷⁻³⁹.

Temperature, oxygen partial pressure, and applied potential have been shown to affect dopant segregation. The equilibrium defect concentrations in the bulk and at the surface are a function of temperature⁴⁰. In addition, high temperatures are required to overcome the high migration barriers ranging from 2.0 eV to 4.0 eV for the diffusion of dopants^{33, 41-42}. The former argument is of a thermodynamic nature, while the latter is about the kinetics. We may conclude that high temperatures are a prerequisite for dopant segregation to occur, but this does not imply that segregation is more (thermodynamically) preferred at higher temperatures. The gas environment, in particular the oxygen partial pressure, influences degradation behavior through the oxygen nonstoichiometry of the electrode material. In addition, the surface precipitate being an oxide, such as SrO, connects segregation to oxygen chemical potential, regardless of the electrode oxygen nonstoichiometry. Nevertheless, it is currently unclear whether higher or lower oxygen chemical potential promotes segregation. Conflicting results can be found in the literature, reporting either progressive enhancement⁴³ or decrease³³ of segregation thin-film LSM with decreasing oxygen pressures. The results reported in these two studies, however, are limited to relatively narrow pressure ranges and small number of sampling points. In our earlier work, Lee *et al.*³³ we have hypothesized that two independent driving forces, the electrostatic and elastic energy of dopants in the lattice, could affect dopant segregation simultaneously at high temperature, but the contribution from the electrostatic contribution was not possible to isolate experimentally. In LSC and related oxides, a broader range of oxygen chemical potentials has been studied using electrochemical polarization⁴⁴⁻⁴⁶, resulting in an increase in segregation for cathodic polarization

of the electrode. The large gap in ionic conductivity between LSC and LSM^{33, 47}, however, prohibits simply generalizing conclusions for LSC to all types of perovskite cathode materials⁴⁸. The polarization also influences the oxygen content of perovskite oxides and affects their segregation behavior. However, extensive amount of contradicting results can again be found in the literature. For thin-film LSM, la O' *et al.* observed an increase in Sr segregation with cathodic polarization⁴⁹ while Huber *et al.* observed the opposite⁵⁰⁻⁵¹. Such contradicting results can also be found in the porous LSM system⁵²⁻⁵⁴. Not only LSM, but also other perovskite oxides, such as (La,Sr)(Co,Fe)O₃, suffer from the same issue⁵⁵⁻⁵⁶. We thought that an in-depth understanding of the connection between polarization and the oxygen chemical potential in perovskite oxide was necessary to explain how driving forces behind segregation change with polarization.

In the present report we use electrochemical polarization to systematically assess the role of oxygen chemical potential in the segregation of dopants to the surface, probing a range from highly reducing to highly oxidizing conditions. In the analysis, we establish a connection to the two reported driving forces behind segregation. We employ a recently developed electrochemical cell configuration utilizing a polarization gradient⁵⁷ across a thin-film electrode to obtain a large range of anodic or cathodic oxygen chemical potentials on one single sample. We obtain effective oxygen pressures spanning a range from 10⁻¹⁶ to 10¹⁵ atm. By selecting the three dopant cations, Ca, Sr, and Ba, with the same charge (2+) but different cation sizes ($R_{Ca}=1.34 \text{ \AA} < R_{Sr}=1.44 \text{ \AA} < R_{Ba}=1.61 \text{ \AA}$), we probe the effects of the misfit elastic energy created by the dopants' size mismatch with respect to the host cation La³⁺. The connection between the dopant size, oxygen chemical potential and segregation is established quantitatively by performing density-functional theory (DFT)-based ab-initio thermodynamics calculations.

These two variables, the dopant cation size and the oxygen chemical potential, are closely related to the two predominant mechanisms behind segregation of dopant cations on this type of perovskite oxides reported in the literature: minimization of the elastic energy (E_{ela}) and the electrostatic energy (E_{elec}) of the dopant cation in the perovskite lattice³³. The elastic contribution originates from the mismatch between the preferred lattice size of the dopant versus the host lattice. The electrostatic energy arises from the attraction of the negatively charged dopants (D^{2+} on a La³⁺ site) to the surface enriched with positively charged oxygen vacancies (V_O^{\bullet}). For example on the La_{0.9}Sr_{0.1}MnO₃ (001) surface, the oxygen vacancy concentration was reported to exceed the bulk

value by a factor of approximately 10^6 under typical SOFC operation conditions, and to exhibit a further increase by three orders of magnitude upon decreasing the oxygen pressure to 10^{-15} atm⁵⁸. Similar differences between the surface and bulk oxygen vacancy concentrations can also be found in other perovskite oxides, including LaCoO_3 ⁵⁹, LaFeO_3 ⁵⁹, LaNiO_3 ⁵⁹, and SrTiO_3 ⁶⁰. The altered bonding environment at the surface affects the formation energy of defects – in this case the formation of oxygen vacancies is facilitated at the surface, which has also been reported for several binary oxides including CeO_2 ⁶¹⁻⁶², rutile TiO_2 ⁶³, and MnO_2 ⁶⁴. Based on the excess of oxygen vacancies at the surface under increasingly reducing conditions, we propose that E_{elec} increases with a decrease in oxygen pressure ($p\text{O}_2$), and we test this hypothesis in our experiments. Understanding the electrostatic driving force from theory requires dedicated computations related to the interactions of surface oxygen vacancies with the dopant, which will be published elsewhere⁶⁵.

On the other hand, we propose that the elastic energy (E_{ela}) affects dopant cations in the bulk and changes their solubilities within the lattice. The cation radii of the chosen dopants here are not the same as that of the host. Ca^{2+} is smaller than the host cation La^{3+} (by -1.5 %), and Sr^{2+} and Ba^{2+} are larger by +5.9 % and +18.4 %, respectively. Based on this, the relative stabilities of the dopants in the perovskite lattice decrease along the Ca, Sr, Ba series. As we will outline in the following, our polarization measurements allow us to probe the chemical potentials of the dopants in the bulk (and thereby the elastic energy) by determining the onset of segregation under anodic polarization. For that, we propose that the enrichment of the dopant at the surface is in part caused by chemical reactions of the dopant with oxygen from the environment. These reactions can result in the formation of dopant oxide and peroxide, either in the form of particles on the surface⁶⁶⁻⁶⁷ or monolayers covering the entire surface⁶⁸⁻⁶⁹. And the reactivity of the dopant to form these precipitates increases with larger dopant size mismatch with respect to the host. We can thus predict the oxygen chemical potential where the formation of these reaction products sets in for the three dopants, and show that this onset oxygen chemical potential is correlated with the dopant cation size. In this work, we probe the two segregation mechanisms described above as a function of oxygen chemical potential modulated by electrochemical polarization of doped LaMnO_3 electrodes. Using X-ray photoelectron spectroscopy (XPS), secondary electron microscopy (SEM), and atomic force microscopy (AFM), we observe a progressive enhancement of surface segregation under increasing cathodic polarization for all three compounds. This behavior

originates from the electrostatic attraction (E_{elec}) of charged dopants to the surface, which is enriched in oxygen vacancies under reducing conditions. Under anodic polarization, segregation is driven by chemical reactions between the dopant cations and gas phase oxygen. The reactivity of dopant cations is enhanced by lattice misfit strain (E_{ela}) of the large dopant cations, as predicted by our ab initio thermodynamics calculations and observed experimentally here for Sr and Ba, in the form of an increase in segregation for LBM and LSM under anodic conditions. Clear differences in the transition point between the elastically and electrostatically dominated regimes demonstrate the balance between these two driving forces and their response to changes in the oxygen chemical potential. Thus, the report at hand provides a systematic analysis of the role of polarization and effective pO_2 in segregation processes on perovskite oxides, and advances the understanding of their driving forces in both reducing and oxidizing conditions.

2. Experimental Methods

Dense thin-film $\text{La}_{0.8}\text{Ba}_{0.2}\text{MnO}_3$ (LBM), $\text{La}_{0.8}\text{Sr}_{0.2}\text{MnO}_3$ (LSM), and $\text{La}_{0.8}\text{Ca}_{0.2}\text{MnO}_3$ (LCM) electrodes were prepared using pulsed laser deposition (PLD) from each target composition, onto commercial (100)-oriented single crystals of yttria-stabilized zirconia (YSZ, 8 mol% Y_2O_3 , from MTI Corp.). When referring to these doped lanthanum manganite films at a collective level, we will denote them as $\text{LDM}=\text{La}_{0.8}\text{D}_{0.2}\text{MnO}_3$ ($\text{D}=\text{Ca}, \text{Sr}, \text{or Ba}$). The film thickness of approximately 80 nm was measured using a Bruker DXT Stylus profilometer. All the thin-film electrodes were deposited at a substrate temperature of 700°C in 0.5 mTorr O_2 and cooled down to room temperature in 500 mTorr O_2 . Before the growth process, the backside and one edge of the YSZ crystals were coated with porous Pt by applying Pt paint (SPI Corp.) and heating at 700°C in air for 30 min to evaporate the solvent and form a solid layer. This configuration establishes a connection between the back side of the electrolyte and a sputter-deposited Pt stripe in contact with one side of the perovskite film (**Figure 1**). The painted Pt layers, connecting the back, edge, and upper region of the YSZ crystals, are used as a counter electrode in the polarization experiments. This configuration enables us to establish a continuous gradient in polarization in the lateral direction at the film surface (see description below). After the thin-film growth, electrical contact points were created using sputter deposition of a Ti adhesion layer (10 nm) followed by a Pt contact layer (100 nm). The regions for sputtering were defined by a Kapton mask which covered the film surface, leaving a 2 mm-gap at the side for depositing the upper side of the counter

electrode. The working electrode was deposited through a $3 \times 7 \text{ mm}^2$ -sized rectangular opening of the mask at a distance of 3 mm from the counter electrode. In order to remove pre-existing surface segregate layers, which form at the surface during PLD deposition, the thin-film samples were immersed in high-purity deionized water for 1 min. This process selectively removed the surface species without significantly compromising the nominal dopant amount in the perovskite phase (**Figure S1** in the Supporting Information). The crystallographic orientations of the thin films were characterized by out-of-plane X-ray diffraction (XRD; Rigaku Smartlab).

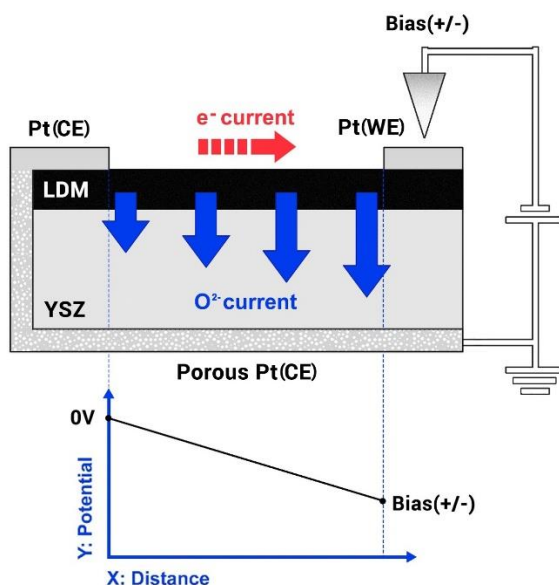


Figure 1. Illustration of the experimental setup designed for applying a continuous polarization gradient across the top electrode surface ⁵⁷. CE=counter electrode; WE=working electrode; LDM= $\text{La}_{0.8}\text{D}_{0.2}\text{MnO}_3$ (D=Ca, Sr, or Ba); YSZ= Y_2O_3 stabilized ZrO_2 , 8% mole Y_2O_3 . The bias voltage applied between the two Pt electrodes leads to a monotonous decrease of the voltage difference applied across the LDM film, illustrated with the schematic potential-distance plot. The resulting lateral gradient of the oxygen chemical potential is reflected in a gradual variation of the pO_2 -dependent surface properties.

The setup for the simultaneous probing of a range of polarization (**Figure 1**) is based on the recent design by Huber *et al.* ⁵⁷. The sample bias is applied to a Pt contact sputtered onto the

electrode film, while the counter electrode (CE), the porous Pt layer on the backside of the YSZ electrolyte, is connected to ground. In contrast to a traditional CE, this model electrode is in electrical contact with a stripe of Pt on the working electrode (WE) side of the electrolyte crystal, connecting it to the thin-film electrode. This contact is established by connecting the porous Pt CE to the sputtered Pt contact across one edge of the electrolyte. The other Pt contact point is used to apply voltage to the WE; it does not have any direct connection to the electrolyte or the CE. In this configuration, the thin-film electrode responds to a potential difference similar to an Ohmic resistor, resulting in a linear voltage drop across the distance between the two electrodes (CE and WE on the top). The requirement for this condition is that the whole region of the electrode surface should be electrochemically active so that the ionic current is not drained solely through the near-WE region; this condition is met when electronic current is far higher than ionic one ($I_{\text{elec}} \gg I_{\text{ion}}$). Huber *et al.*⁵⁷ showed that LSM had appropriate electronic and ionic properties which satisfied such condition. We have also confirmed the presence of a linear potential variation across the film surface, by *in-situ* core level photoemission measurements of LSM under polarization (**Figures S2 and S3** in the Supporting Information). These measurements have shown a linear shift in the binding energy position of the core level peak of La 4*d* taken at different lateral positions on the LSM film. Thus, applying a bias voltage between the WE and CE (ground) creates a gradient in the electric potential, monotonically changing across the film surface from the full applied voltage at the WE contact to 0 V at the CE contact on the film electrode. As a result, the differences in both the electric potential as well as the oxygen chemical potential between the CE and WE cover a continuous range from 0V up to the full applied voltage. This novel experimental setup allows us to use one single sample to probe the effect of a large range of bias voltages. This not only saves time, but also eliminates possible variations between experimental conditions and sample history, such as film thickness, deposition temperature, or pO_2 , which can differ slightly between samples and preparations. In such a configuration, we have also confirmed that the Joule heating that may arise from lateral electronic current does not affect the temperature profile, because it is offset by forced convection in O₂ gas flow (see Supporting Information for details).

For each compound, +800 mV, 0 V, and -800 mV were applied to the WE of three separate thin-film electrode samples. According to the Nernst equation, these potential values correspond to effective oxygen pressures of 10^{15} , 10^0 , and 10^{-16} atm, respectively. One additional sample from each PLD-grown set was reserved as an as-prepared reference sample. The local cation

composition at four to five points (± 160 , ± 320 , ± 480 , ± 640 , -750 mV) between the two electrodes was analyzed by X-ray photoelectron spectroscopy (XPS) using a Physical Electronics Versaprobe II X-ray photoelectron spectrometer equipped with a monochromated Al K α X-ray source. The distance between each point is constant, corresponding to equal potential steps of 160 mV, as supported by the photoemission peak shifts in **Figure S2** measured *in-situ* while applying negative potential to LSM. *Ex-situ* samples were prepared by heating the films under electrical polarizations for one hour at 770 °C in an atmosphere of 1 atm O₂ in a tube furnace. For quantitative analysis, core-level emission lines with similar inelastic mean free paths (λ) were chosen (see Supporting Information for details); these are La 4*d* ($\lambda = 1.7$ nm); Mn 3*p* ($\lambda = 1.7$ nm); Ba 4*d* ($\lambda = 1.7$ nm); Sr 3*d* ($\lambda = 1.6$ nm); Ca 2*p* ($\lambda = 1.4$ nm)⁷⁰. The angle between the analyzer and the surface plane was set to 45°. The spectra were analyzed to quantify the amount of each component by normalizing their peak area by the sensitivity factor of each core-level orbital⁷¹. For LSM, also *in-situ* ambient-pressure XPS (APXPS) experiments were performed in 100 mTorr O₂ at 650°C using the configuration described above at the beamline TEMPO at the synchrotron facility SOLEIL (France). A detailed explanation of the obtained *in-situ* data and its implications is provided in the Supporting Information.

The surfaces of the films were imaged using high-resolution scanning electron microscopy (HRSEM) and atomic force microscopy (AFM) to reveal the morphology of the surface segregates, which typically precipitate out as particles. HRSEM was measured by a Zeiss Merlin HRSEM with an in-lens secondary electron detector. AFM measurements were performed using a Veeco Metrology Dimension 3100 AFM with a Nanoscope V controller (tapping mode), as well as a Park NX-10 AFM operated in non-contact mode.

3. Computational Approach

The density functional theory (DFT) calculations were performed using the Vienna Ab-initio Simulation Package (VASP)⁷² using the PBE functional⁷³ with Hubbard-U correction (Dudarev's approach)⁷⁴ of 4 eV on the Mn 3*d* orbital³³. The ferromagnetic, half-metallic state was reliably reached by setting MAGMOM to 3.5 for Mn. For bulk and surface computations meshes of $(6 \times 6 \times 4)$ and $(6 \times 6 \times 1)$ k-points were chosen for primitive orthorhombic cells (corresponding to $(\sqrt{2} \times \sqrt{2} \times 2)$ super cells of the cubic structure) and surface slabs, respectively. Together with an energy cutoff of 550 eV this approach ensures convergence of total

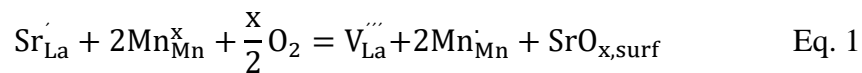
energies and bulk vacancy formation energies within 4 meV/atom. To reliably study surface segregation we model the surface in a symmetric slab with 15 and 17 layers for the MnO₂ and AO terminations, respectively, corresponding to 7.5-8.5 ABO₃ bilayers. Surface free energies and segregation energies are converged with respect to the slab thickness within 0.9 meV/Å² and 7 meV, respectively.

A well-known problem in the modeling of oxides arises from the overbinding of oxygen in the gas phase versus the bulk oxide. This error can be corrected by applying Wang's scheme⁷⁵ of fitting the deviation between computed and experimental formation energies of binary oxides. The O₂ overbinding correction in our case amounts to +1.03 eV.

3.1. Dopant segregation model

We study the segregation of dopants in LCM, LSM and LBM over a wide range of cathodic and anodic potentials and propose an elastic and an electrostatic driving force to compete, with the elastic driving force to dominate under oxidizing conditions (anodic polarization) and the electrostatic driving force competing under reducing conditions (cathodic polarization). The segregation under reducing conditions will be studied by theory in a forthcoming publication⁶⁵ and we limit our theoretical considerations at this point to oxidizing conditions (anodic potential). We propose that dopants can undergo chemical reactions with oxygen from the gas phase, which are driven by the high oxygen chemical potential under these conditions. However, the driving force to undergo such reactions is directly connected to the elastic energy of the dopant dissolved in the LaMnO₃ host lattice, and we will exploit this connection to explain the different segregation behavior we observe for the three samples under anodic polarization as shown below.

Let us consider the chemical reactions of a Sr dopant cation with O₂ from the gas phase, forming SrO_x:



The dominant charge compensation mechanism in doped lanthanum manganites is valence change of Mn. In Kröger-Vink notation, Mn'_{Mn} , Mn^x_{Mn} and $\text{Mn}^{\cdot}_{\text{Mn}}$ indicate Mn²⁺, Mn³⁺ and Mn⁴⁺. The introduction of negatively charged A-site vacancies is therefore accompanied by oxidation of Mn³⁺ (Mn^x_{Mn}) to Mn⁴⁺ (Mn[·]_{Mn}).

The Gibbs free energy of this reaction is given by the difference between the free energy of SrO_x , $G_{\text{SrO}_x, \text{surf}}$, and the sum of oxygen chemical potential, $\frac{x}{2} \mu_{\text{O}_2}$, and cation chemical potential, μ_{Sr} . Since this reaction requires gas phase oxygen, its Gibbs free energy is a function of the oxygen chemical potential with a slope of $-\frac{x}{2}$:

$$\Delta G(T, p\text{O}_2) \approx G_{\text{SrO}_x, \text{surf}}(T, p\text{O}_2) - \frac{x}{2} \mu_{\text{O}_2}(T, p\text{O}_2) - \mu_{\text{Sr}}(T, p\text{O}_2), \quad \text{Eq. 2}$$

This means that formation of SrO_x (grown either in the form of a particle or as a monolayer) is favored at higher oxygen chemical potentials. The cation chemical potential contains an elastic energy contribution, E_{ela} , which depends on the cation size mismatch. ΔG can be positive or negative for the above equation, which either indicates that the dopant is stable (soluble) in the lanthanum manganite lattice (ΔG positive), or will precipitate as a binary oxide (ΔG negative). The conditions $(T, p\text{O}_2)$ where ΔG is equal to 0 will therefore be called the onset of precipitation. The precipitation onset to be determined experimentally is directly relatable to the dopant chemical potential (and thereby the elastic energy) because the other two terms ($G_{\text{SrO}_x, \text{surf}}(T, p\text{O}_2)$ and $\mu_{\text{O}_2}(T, p\text{O}_2)$) are known in our polarization experiment. Determining the electrochemical polarization at the onset of dopant oxide segregation thereby allows us to probe the elastic energy of the dopant cation

We consider both the precipitation of dopant oxides and peroxides in the form of particles, as well as the formation of epitaxial monolayers. The formation energies for the earth alkali oxides and peroxides are given in **Table S1** in the supporting material. The oxide and peroxide precipitation thermodynamics are independent of film orientation as only bulk properties (dopant cation chemical potential, formation energy of dopant oxide and peroxide) enter the equation. Additionally, we consider the formation of wetting films of dopant oxide and peroxide monolayers growing on the surface. To capture the trends of film wetting within the (Ca, Sr, Ba) series, we shall consider monolayers of the oxide and peroxide grown homoepitaxially on the (001)-oriented LDM surface on top of the MnO_2 termination.

3.2. Computation of chemical potentials

We model the exchange of cations between surface and bulk as a Schottky defect reaction, where cations from the bulk migrate to the surface to occupy empty lattice sites or form a

precipitate, as given by **Error! Reference source not found.**, the energy cost of moving a cation from the bulk to the surface is therefore connected to the bulk vacancy formation energy and can be expressed as a chemical potential as given by Eq. 2. For the cations, Ca, Sr, Ba, La, and Mn, the chemical potentials were calculated from bulk DFT energies as

$$\mu_i = \left(\frac{dG_{bulk}}{dn_i} \right)_{j \neq i} \approx \left(\frac{dE_{bulk}}{dn_i} \right)_{j \neq i}, \quad \text{Eq. 3}$$

neglecting entropy contributions. These energies are calculated in bulk super cells with 64 ABO_3 units, where a dopant concentration of 20 % (LDM) approximately corresponds to the composition $\text{La}_{51}\text{D}_{13}\text{Mn}_{64}\text{O}_{192}$. The compositional change upon removal of one cation is $1/64 \approx 1.6\%$, so that we can approximate the derivative on the total energy by the cation number n_i as the difference between the defect-free LDM unit cell (E_{LDM}) and an LDM unit cell with one atom i removed ($E_{LDM,def,i}$), keeping the number of all other ions (denoted by j), constant. The chemical potential referenced to the gas phase energy of atom i ($E_{gas,i}$):

$$\mu_i \approx \left(\frac{dE_{bulk}}{dn_i} \right)_{j \neq i} \approx E_{LDM,def,i} + E_{gas,i} - E_{LDM}. \quad \text{Eq. 4}$$

Since the total energy of a bulk unit cell depends on the arrangement of point defects and dopants within the unit cell, each energy $E_{LDM,def,i}$ and E_{LDM} was calculated four times for different random configurations in a large supercell (64 units) and the average was taken. From the scatter of total energies we estimate that the relative error of the chemical potential difference between the different dopants is less than 0.2 eV.

The oxygen chemical potential μ_{O_2} is computed from the standard oxygen chemical potential $\mu_{O_2}^0$ as a function of temperature (obtained from the NIST database ⁷⁶):

$$\mu_{O_2}(T, p_{O_2}) = \mu_{O_2}^0(T) + k_B T \log \left(\frac{p_{O_2}}{p^0} \right) \quad \text{Eq. 5}$$

4. Results

4.1. Structure of dense thin-film electrodes:

After deposition and pre-treatment with deionized water, the films were characterized using out-of-plane X-ray diffraction (XRD) and profilometry. The XRD patterns of the films (**Figure 2**) show clear peaks corresponding to a (110) orientation (cubic indices), with small components arising also from (100) and (111). The sample thickness is within 80 ~ 100 nm (see **Figure S4** in the Supporting Information for details). The surfaces appear smooth without any discernable particles within the scanning electron microscopy (SEM) image resolution (**Figure S5**). XRD patterns acquired after annealing with polarization indicate no change in the present phase and crystal orientation of the films compared to the as-prepared state (**Figure S6**).

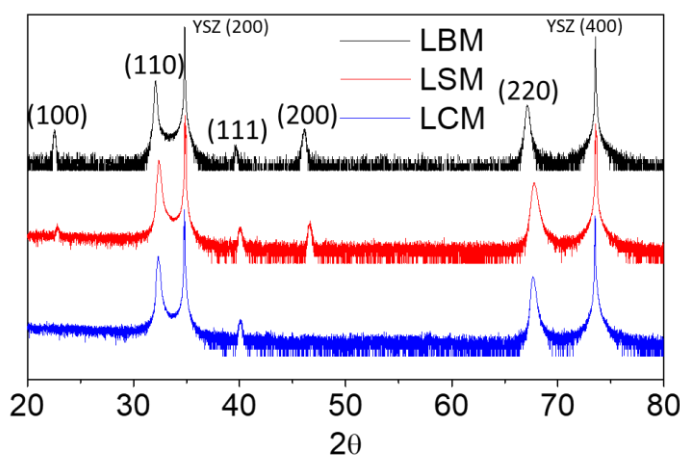


Figure 2. XRD patterns of $\text{La}_{0.8}\text{Ca}_{0.2}\text{MnO}_3$ (LCM, blue), $\text{La}_{0.8}\text{Sr}_{0.2}\text{MnO}_3$ (LSM, red), and $\text{La}_{0.8}\text{Ba}_{0.2}\text{MnO}_3$ (LBM, black).

4.2. Surface chemistry of doped LaMnO_3 film electrodes:

X-ray photoelectron spectra of all constituent elements have been acquired to quantify the dopant segregation behavior on LCM, LSM, and LBM. Ca 2*p*, Sr 3*d*, and Ba 4*d* core-levels have been selected for chemical analysis, because they are known to change significantly with the bonding environment, and thus, have been widely used in previous segregation studies^{33, 36, 48, 77}.

Figure 3 shows characteristic spectra of the respective dopant species for the as-prepared and annealed films. The spectra have been deconvoluted into two Voigt doublet components: a component at high binding energy, which is commonly attributed to the segregated dopant phase at the surface (green), and a lattice component at low binding energy (blue) corresponding to the original perovskite phase. O 1*s*, La 4*d*, and Mn 3*p* core-level spectra were also acquired to quantify

the composition of the surface region (see **Figure S7** in the Supporting Information). As can be seen from **Figure 3** (top) and **Figure S1**, the as-prepared films show low amounts of the respective surface component and the intensity of the lattice component is similar between each other. However, the amount of the surface component for all the dopants is increased after annealing, which indicates the formation of surface oxide phases under oxidizing conditions and at high temperature (**Figure 3**, bottom).

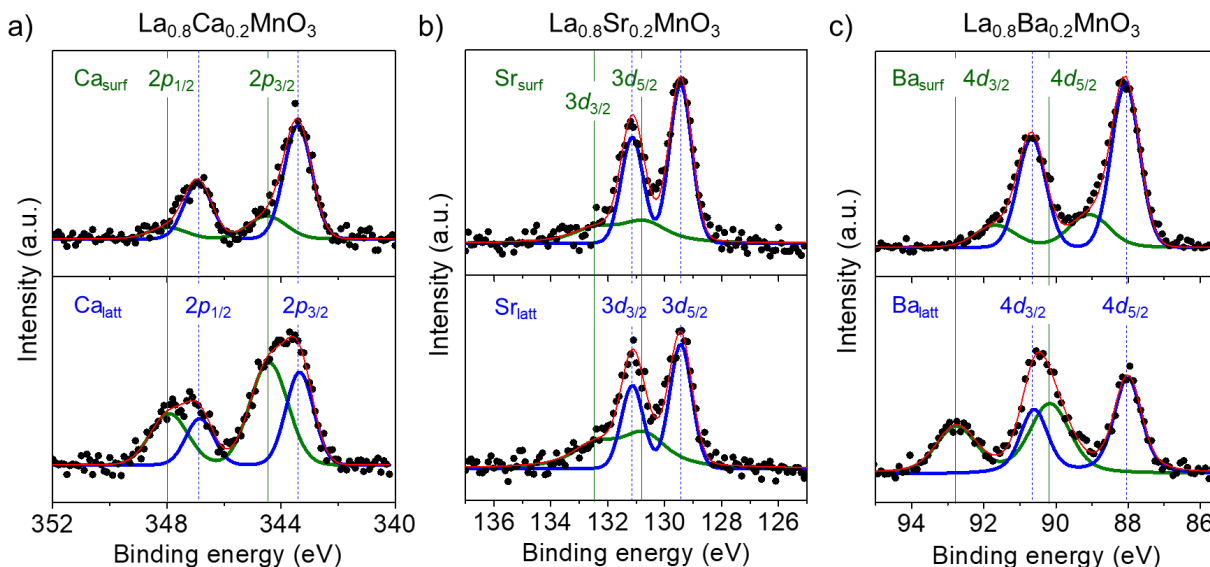


Figure 3. Representative core-level X-ray photoelectron spectra of a) Ca $2p$, b) Sr $3d$, and c) Ba $4d$. $\text{La}_{0.8}\text{Ca}_{0.2}\text{MnO}_3$, $\text{La}_{0.8}\text{Sr}_{0.2}\text{MnO}_3$, and $\text{La}_{0.8}\text{Ba}_{0.2}\text{MnO}_3$ films were annealed in pure O_2 for 1 h at 770°C ; no bias was applied on the samples shown here. The spectra of the respective as-prepared (top) and annealed (bottom) films were deconvoluted to show lattice (blue) and surface (green) species.

In virtue of the lateral polarization method, only two films were required to take 9 different sets of spectra in this experiment, eliminating errors that could result from possible differences in sample preparation history. As shown in **Figure S2**, the existence of a linear potential gradient on an LSM film is demonstrated by the corresponding linear energy shift of the La $4d$ peak with lateral position at the surface, measured *in situ* with polarization of the sample at the synchrotron. **Figure 4** describes the progressive changes in each dopant core-level spectrum (Ca $2p$, Sr $3d$, and Ba $4d$) ranging from positive (red) to negative (blue) potentials. Given the positions at which these spectra were taken at the surface, and the linear relation of potential to position (**Figure S2**), the

corresponding potentials are assigned as ± 160 mV, ± 320 mV, ± 480 mV, ± 640 mV, -750 mV. The intensity of each spectrum was normalized by the amount of total A-site cations. By deconvoluting each spectrum as illustrated in **Figure 3**, the respective surface components in the spectra, the amount of Ca_{surf} , Sr_{surf} , and Ba_{surf} , can be quantified as a function of the local electrochemical potential.

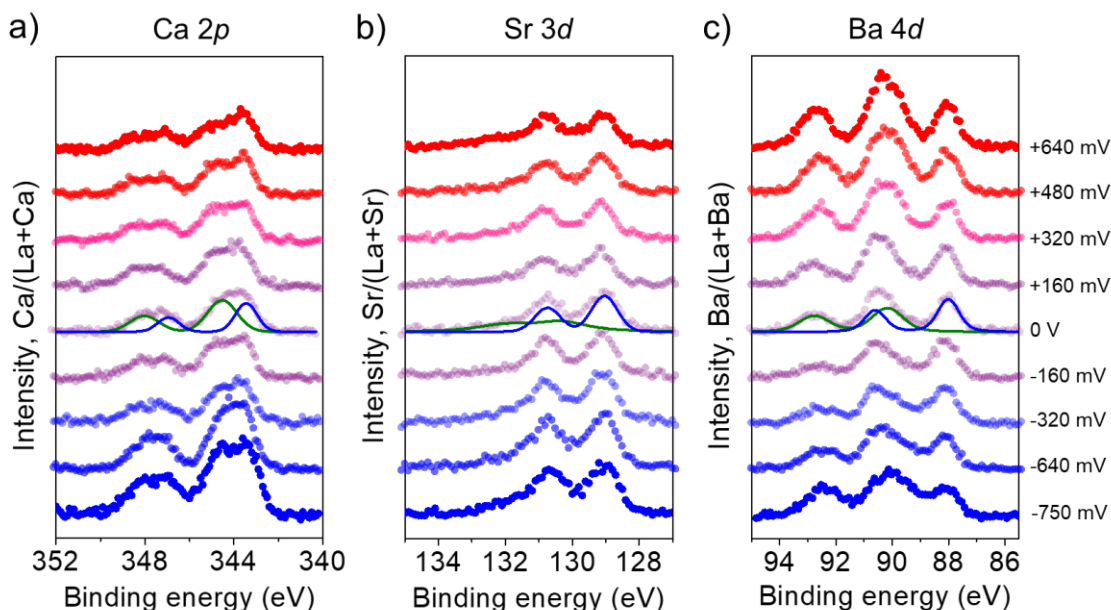


Figure 4. X-ray photoelectron spectra taken for Ca $2p$, Sr $3d$, and Ba $4d$ illustrating the extent of dopant segregation at the surface as a function of applied potential at 770°C in 1 atm O_2 for 1 h on a) $\text{La}_{0.8}\text{Ca}_{0.2}\text{MnO}_3$, b) $\text{La}_{0.8}\text{Sr}_{0.2}\text{MnO}_3$, and c) $\text{La}_{0.8}\text{Ba}_{0.2}\text{MnO}_3$. The 0 V spectrum in each core-level is deconvoluted into the components arising from the surface (green) and lattice (blue) binding environments.

Figure 5 shows the intensity of the respective surface components of Ca $2p$, Sr $3d$, and Ba $4d$. This data was obtained by deconvoluting the surface components (green curves) shown in **Figure 4**, and normalized by the total peak area of the A-site cations, plotted as a function of applied potential. On all three compounds, the surface contribution of the dopant increases towards higher negative polarization values within a particular potential range: +640 mV to -750 mV for LCM, +160 mV to -750 mV for LSM, and -160 mV to -750 mV for LBM. The ranges vary substantially between the three compounds, as seen by the clear shift of the point of minimum segregation. In the cases of LSM and LBM, the segregation also increases with increasing anodic polarization,

leading to a minimum in the potential-dependent intensity of the surface component. A monotonic increase in segregation is observed from +160 mV to +640 mV for LSM and -160 mV to +640 mV for LBM. The segregation curves exhibit a sharp transition point, a minimum in the cases of LSM (at +160 mV) and LBM (at -160 mV). The corresponding potential of minimum segregation shifts towards more negative values with increasing dopant radius, from Sr to Ba. For LCM, there is only a change between a steep and a flat potential-dependence of segregation (at -480 mV). In addition, the variation in the total amount of each dopant (D) and that of the lattice component (D_{latt}) with respect to the applied potential is plotted in **Figure S8**. **Figure S8a** shows that the total amount of Ca increases at high cathodic bias while for Ba this is observed at anodic bias, which clearly indicates the respective dominant driving force of segregation in each compound. As can be seen in **Figure S8b**, $D_{\text{latt}}/(La+D)$ of each compound becomes suppressed compared to the as-prepared samples across a wide range of potentials. We think this is because dopants segregated as particles cover the surface, while a large amount of dopants in the perovskite oxide phase could not be measured by the surface-sensitive technique XPS. For LSM, the cathodic regime has also been investigated using *in-situ* XPS at 650°C in 100 mTorr O₂ with an applied voltage of up to -600 mV (Supporting Information). As seen in the core level spectra (**Figure S3**) the contribution of surface Sr grows monotonically with increasing cathodic polarization.

To further confirm the validity of these results, we also examined the segregation behavior of LCM and LBM by applying four different constant potentials on four individual films and checked if the segregation amount on each sample is consistent with the segregation curve (**Figure 5a** and **5c**) drawn by using the lateral polarization method. We chose -600 mV, -150 mV, +300 mV and +900 mV to test this (**Figure S9** and **S10**). As a result, the amount of Ca_{surf} monotonically decreased throughout the negative potential region up to +300 mV, which matches well with the result from the lateral polarization experiment. Constant polarization on LBM samples also showed similar results with the lateral polarization experiment, with a non-monotonic dependence on polarization and a minimum segregation point close to -150 mV. The sudden increase in Ca_{surf} at +900 mV indicates that LCM also begins to react with gaseous oxygen at higher anodic polarizations. Detailed explanation on this is provided in the Discussion section.

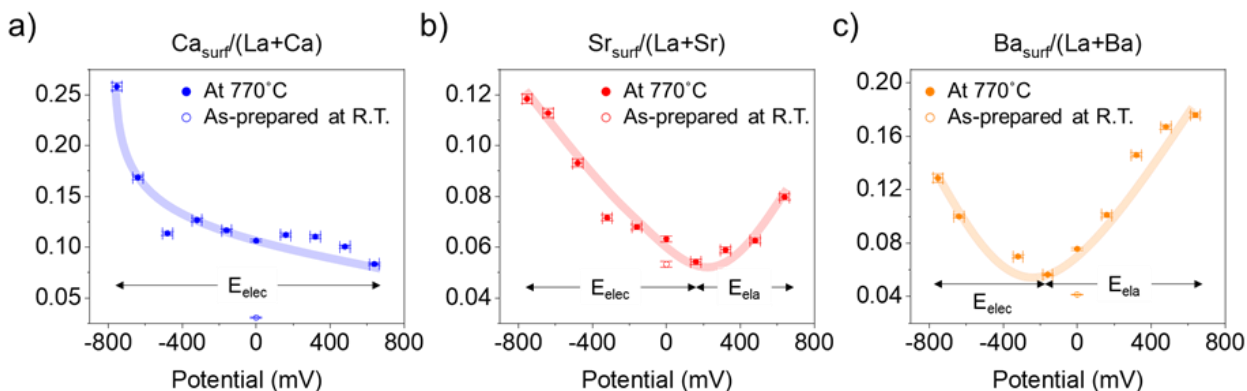


Figure 5. XPS intensity of surface a) Ca, b) Sr, and c) Ba components, normalized by the total intensity of A-site cations of $\text{La}_{0.8}\text{Ca}_{0.2}\text{MnO}_3$, $\text{La}_{0.8}\text{Sr}_{0.2}\text{MnO}_3$, and $\text{La}_{0.8}\text{Ba}_{0.2}\text{MnO}_3$, respectively. The filled circles indicate the data points from the polarized samples annealed at 770°C in 1 atm O_2 for 1 h. The open circles indicate the data points from the as-prepared samples. The arrows in the graphs indicate the regions where the electrostatic energy or elastic energy is the dominant reason of segregation of the dopant. The thick trend lines serve only as a guide to the eye. A detailed explanation on the calculation of the error bars associated with each data point is available in the Supporting Information Section S8.

4.3. Surface morphology of doped LaMnO_3 thin-film electrodes:

The differences in surface topography due to dopant segregation have been analyzed by SEM and AFM, as shown in **Figures 6, S11, and S12**. For LSM and LBM, the surface at the highest negative (cathodic) potential (-750 mV) is populated by small particles (**Figure 6**). However, the species on LCM exhibit a granular structure consisting of particles of similar size, covering its entire surface. Under the most positive (anodic) potential (+640 mV), the surfaces of LSM and LBM are characterized by the formation of smaller particles than those under the negative potential, whereas LCM does not exhibit any discernible features. Further SEM images of LSM and LBM were acquired under the potentials showing the lowest segregation in XPS, +160 mV and -160 mV, respectively. For LCM, +160 mV was selected as an intermediate step. Also, the area coverage of the surface particles on each surface is compared by using a brightness filter that selectively calculates the area covered by the particles (**Figure S11**).

The influence of the applied potential on the surface roughness has been also been assessed using AFM. **Figure S12** summarizes the AFM results and provides a comparison of the three

compounds. Images (a-c) illustrate the surface topography after annealing at high negative (-670 mV) and positive (+670 mV) potentials in pure O₂ for 1 h at 770°C. Tiny particles observed by SEM on the most positive side of LBM (the inset in **Figure 6c**, right) were not observed by AFM. Graphs at the bottom of **Figure S12** show the trend in roughness values from the matrix phase (particle free zones) of each film surface. The root-mean-square (RMS) roughness (blue line) shows a clear common trend towards smoother surfaces at positive potentials for LCM and LBM. Especially for LCM, the evolution of surface roughness matches well with the evolution of Ca_{surf} as quantified by XPS in **Figure 5**. However, LSM does not exhibit any clear trend in the roughness and very little overall variation. The large error bar for LCM at -670 mV results from a coexistence of rough and flat patches at the surface.

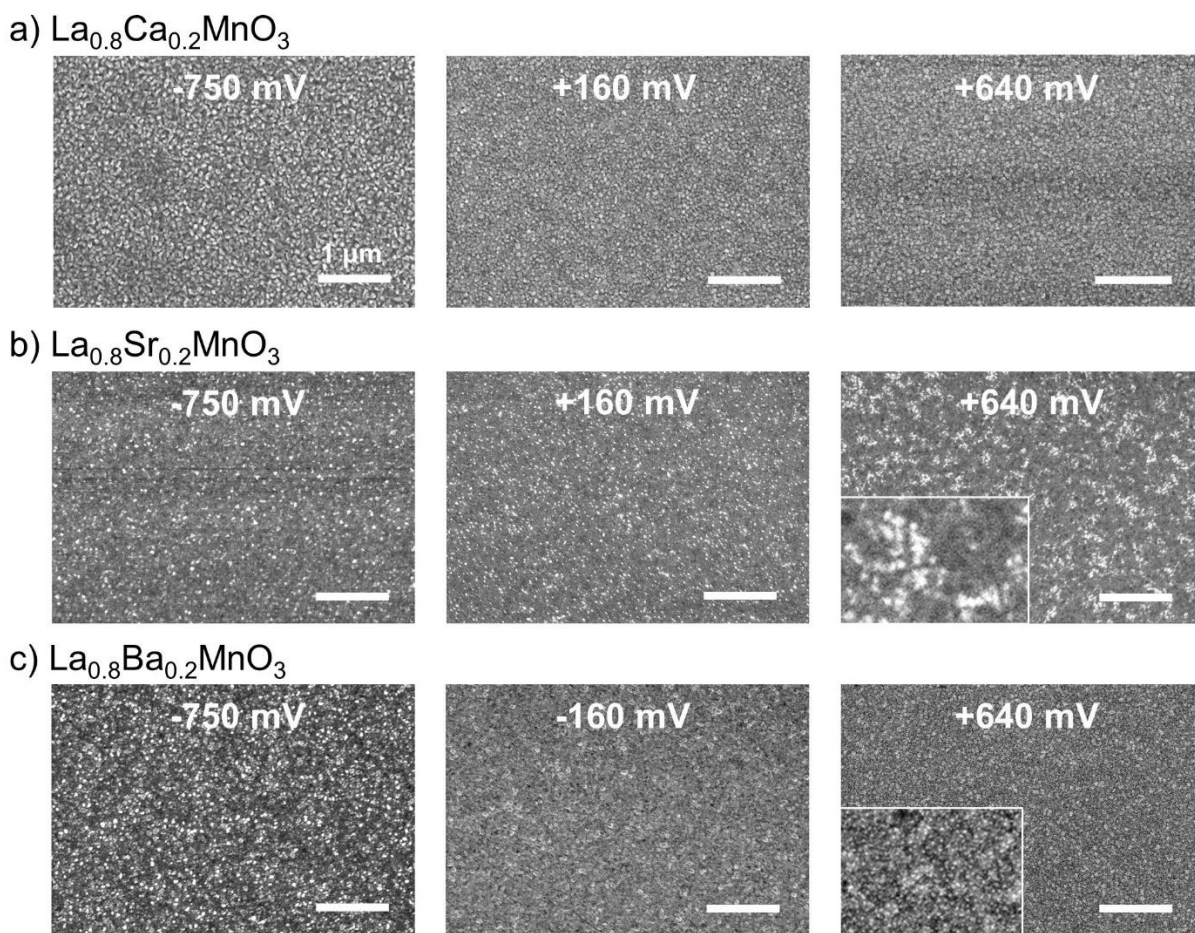


Figure 6. SEM images of the La_{0.8}Ca_{0.2}MnO₃, La_{0.8}Sr_{0.2}MnO₃, and La_{0.8}Ba_{0.2}MnO₃ surfaces after annealing at 770°C in 1 atm O₂ under polarization, acquired at different locations

corresponding to the indicated bias voltages. a) $\text{La}_{0.8}\text{Ca}_{0.2}\text{MnO}_3$ at -750 mV, +160 mV, and +640 mV, b) $\text{La}_{0.8}\text{Sr}_{0.2}\text{MnO}_3$ at -750 mV, +160 mV, and +640 mV, and c) $\text{La}_{0.8}\text{Ba}_{0.2}\text{MnO}_3$ at -750 mV, -160 mV, and +640 mV. The magnification of all the images is 25k with a scale bar indicating 1 μm . Insets in $\text{La}_{0.8}\text{Sr}_{0.2}\text{MnO}_3$ and $\text{La}_{0.8}\text{Ba}_{0.2}\text{MnO}_3$ at +640 mV are 4-times further magnified images for a clearer view of small particles on their surface.

4.4. Trends in segregation for different earth alkali dopants on the A-site rationalized by theory

The cation size mismatch between dopant and host cations has previously been considered as an indicator for an increased tendency of A-site dopants to enrich at the surface for elements within the earth alkali metal series (Ca, Sr, Ba)³³. One of the main results of the study by Lee *et al.* was that cation surface enrichment is strongly correlated with the ionic radius, both experimentally and on first-principles level³³. While the resulting segregation energies as a function of cation radius are generally consistent with intuition, a connection between segregation and thermodynamic variables, such as T , $p\text{O}_2$, or applied potential is needed for quantitatively confirming this theory and linking it to our polarization experiments. This connection can be established by considering the chemical potentials of the cations in the bulk, which indicate how easily these cations undergo chemical reactions with the O_2 environment in the sense of **Error! Reference source not found.**. The chemical potentials for the dopant cations Ca, Sr and Ba and host cations La and Mn in LCM, LSM and LBM at 20 % doping level calculated by DFT according to Eq. 3 are listed in **Table 1**. The total variation for the chemical potentials within this series is 0.14 eV, 0.46 eV and 0.83 eV for Mn, La and the dopant D, respectively. All the chemical potentials increase with increasing the dopant size, except for μ_{Mn}^0 , which is identical for LSM and LBM. The overall increase of chemical potentials with respect to dopant cation radius reflects the decreasing stability of the LCM, LSM and LBM compounds with increasing dopant size. This result is in accordance with our hypothesis that the elastic energy contribution increases with dopant cation radius.

Table 1. Cation chemical potentials in stoichiometric 20 % (Ca, Sr, Ba)-doped LaMnO_3 calculated with respect to atomic reference (in eV).

Compound			
	$\text{La}_{0.8}\text{Ca}_{0.2}\text{MnO}_3$	$\text{La}_{0.8}\text{Sr}_{0.2}\text{MnO}_3$	$\text{La}_{0.8}\text{Ba}_{0.2}\text{MnO}_3$
μ_{dopant}^0	-8.61	-8.22	-7.73
μ_{La}^0	-13.23	-12.91	-12.77
μ_{Mn}^0	-6.81	-6.67	-6.67

In order to correlate these chemical potentials with dopant segregation, we need to consider the proposed driving forces of dopant segregation under reducing and oxidizing conditions. Under reducing conditions (cathodic polarization), we propose that dopant enrichment at the surface is driven by electrostatic attraction between the positively charged oxygen vacancies and the negatively charged dopants (relative to pristine LaMnO_3). This electrostatic driving will be considered in detail in a separate publication ⁶⁵.

Under oxidizing conditions (anodic polarization), we propose that segregation is driven by the formation of binary compounds that are more stable under oxidizing conditions (**Error! Reference source not found.**). This segregation mechanism is related to the cation chemical potentials, which reflect the higher chemical reactivity of larger dopants compared to smaller dopants due to the elastic energy. As the precipitated particles observed in our experiments are large, up to 500 nm in size (cf. **Figure 6**), precipitation under anodic polarization is modeled using only bulk energies. For the dopant dissolved in the perovskite we employ the values given in **Table 1**. For the precipitates (oxides and peroxides) we employ their bulk energies given in **Table S1**. Favorable wetting of the precipitates can reduce the onset of near-surface dopant enrichment and possibly change the relative stabilities of dopant oxides and peroxides wetting the surface, but will not result in the formation of particles observable by SEM. Wetting energies were studied using a (100)-oriented oxide or peroxide film on the (001) surface of the perovskite oxide. Since the wetting energy is controlled by the lattice mismatch between the dopant oxide and the perovskite lattice and both are metrically (near-)cubic, the lattice mismatch is independent of surface orientation. We therefore assume that the wetting energies on the (001) qualitatively reflect the trend between the three dopants even if the experiments are primarily on (110)-oriented perovskite films.

However, we recall again that these wetting energies are irrelevant for the thermodynamics of precipitation as long as the formed particles are sufficiently large.

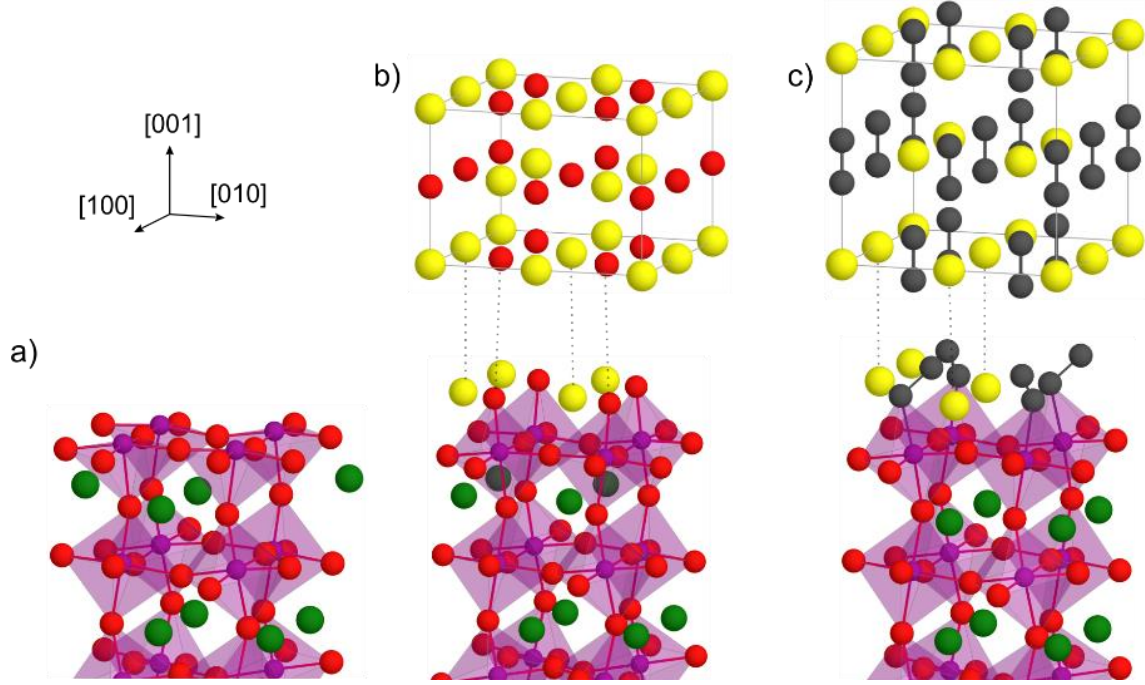


Figure 7. Structures of a) MnO₂, b) SrO, and c) SrO₂ terminations at LSM (001) (bottom) together with bulk structures of SrO (b) and SrO₂ (c) (top). Colors: purple – Mn, green – La, yellow – Sr, red – oxide O²⁻, black – peroxide (O₂)²⁻.

We consider segregation in the form of dopant oxide and peroxide particles, as well as the formation of epitaxial monolayers of oxides and peroxide. **Figure 7** shows models of these surface terminations computed with DFT for the LSM (001) surface. The relative stabilities between the bulk structure and monolayer for compound i with $i = (\text{CaO}, \text{SrO}, \text{BaO}, \text{CaO}_2, \text{SrO}_2, \text{BaO}_2)$ are given by the wetting energy

$$E_{\text{wet},i} = E_{\text{slab},i \text{ term.}} - E_{\text{slab},\text{MnO}_2 \text{ term.}} - E_{\text{bulk},i}, \quad \text{Eq. 6}$$

where $E_{\text{slab},\text{MnO}_2 \text{ term.}}$ and $E_{\text{slab},i \text{ term.}}$ indicate the total energies of surface slabs terminated by a monolayer of the compound MnO₂ and i , respectively, and $E_{\text{bulk},i}$ indicates the total bulk energy of the compound i . The DFT-calculated wetting energies for the earth alkali oxides and peroxides on the LCM, LSM, LBM (001) surface are listed in **Table 2**. The wetting energies are almost universally negative, the only exception being CaO, which has a slightly positive wetting energy

of +0.015 eV. A negative wetting energy indicates higher stability of the homoepitaxial layers compared to the bulk compound, increasing the overall tendency of dopants to enrich at the surface. For the (Ca, Sr, Ba)O series of compounds, the wetting energies are highly correlated with the mismatch, with lower absolute mismatches resulting in more negative wetting energies. The highest negative wetting energy is obtained for BaO with a lattice mismatch of only +0.03 %. This high correlation between lattice mismatch and wetting energy can be explained by the structural similarity between the bulk (Ca, Sr, Ba)O phase and the (Ca, Sr, Ba)O overlayer, which is essentially just one layer of the bulk earth alkali oxide stretched to fit the LSM lattice as illustrated in **Figure 7b**.

This correlation is not found for the peroxide compounds (cf. **Table 2**), where the strongest and weakest wetting is obtained for SrO₂ and BaO₂, respectively, while BaO₂ and CaO₂ have the smallest and largest lattice mismatches. We attribute this lack of trend to the higher flexibility of the peroxide structure regarding lattice expansion. The bulk structure of the earth alkali peroxides is derived from the rocksalt structure by replacing O²⁻ by an (O₂)²⁻ molecular ion with the O—O bond aligned along the [001] direction as shown in the top part of **Figure 7c**. The earth alkali oxide structure is rigid, and lattice expansion requires stretching the cation-O bonds. On the other hand, the O₂²⁻ molecule ion in earth alkali peroxides can be tilted, which allows for lattice expansion without bond stretching (cf. **Figures S13** and **S14**). The tilting of the (O₂)²⁻ molecule ion in the peroxide structure introduces an additional degree of freedom, which makes the peroxide lattice more easily deformable compared to the oxide structure. Therefore, we observe no correlation between lattice mismatch and wetting energy for the peroxide monolayers in contrast to the oxide overlayers.

Table 2. Wetting energies and lattice mismatches for earth alkali metal oxides (CaO, SrO, BaO) and peroxides (CaO₂, SrO₂, BaO₂) on the MnO₂-terminated (001) surface of LCM, LSM and LBM. Lattice mismatches of oxide and peroxide compounds are given with respect to stoichiometric LCM, LSM and LBM.

Dopant	$E_{wet,oxide} / \text{eV}$	oxide lattice mismatch	$E_{wet,peroxide} / \text{eV}$	peroxide lattice mismatch
Ca	+0.015	-13.1 %	-0.345	-16.4 %
Sr	-0.512	-6.4 %	-0.374	-9.4 %
Ba	-0.946	+0.03 %	-0.192	-2.6 %

The free energy of reaction as given by Eq. 2 for the three dopants, including the wetting energy for the homoepitaxial monolayers (Eq. 6) is plotted in **Figure 8a-c** for the three compounds LCM, LSM and LBM. Each diagram shows five lines, representing the dopant in La_{0.8}Ca_{0.2}MnO₃, La_{0.8}Sr_{0.2}MnO₃, La_{0.8}Ba_{0.2}MnO₃, (blue), the bulk oxide (solid orange), and the bulk peroxide (solid green), as well as oxide and peroxide monolayer structures on the surface (dashed orange and green, respectively). As given by the almost universally negative (and μO_2 -independent) wetting energies of oxides and peroxides on the (001) surface of 20 % (Ca, Sr, Ba)-doped LaMnO₃ (cf. **Table 2**), the surface monolayer structures (dashed lines) always show a higher stability than the respective bulk precipitate structures (solid lines). The only exception here is CaO, where the slightly positive wetting energy (given in **Table 2**) indicates that particle and monolayer are equally stable. As a consequence, the stability lines for particle and monolayer overlap (orange line in **Figure 8a**).

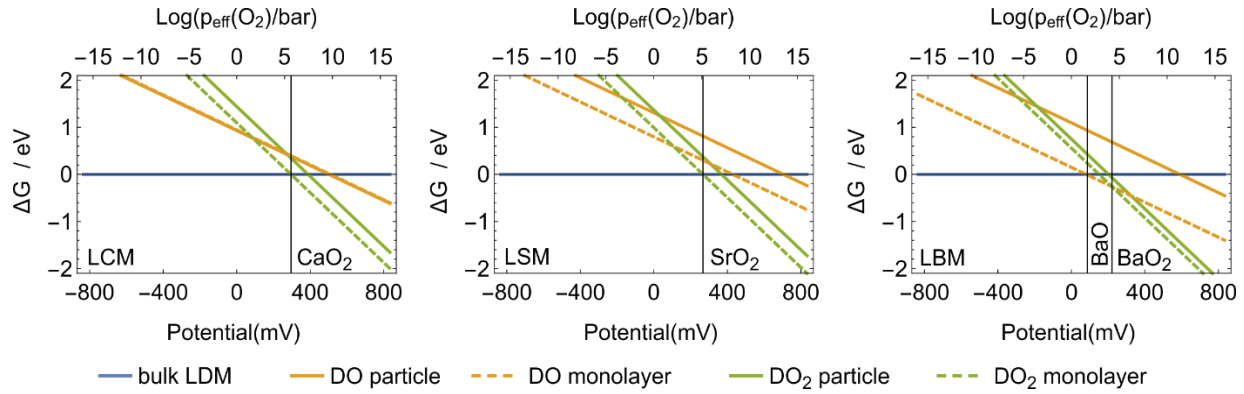


Figure 8. Relative stabilities of the A-site dopant in 20 % (Ca, Sr, Ba)-doped LaMnO_3 bulk (blue), CaO , SrO , BaO (orange) and CaO_2 , SrO_2 , BaO_2 (green). Relative stabilities of oxide and peroxide particles and monolayer structures are given by solid and dashed lines. Regimes of the stable phases are separated by black vertical lines, and the most stable phase is indicated by labels in the plots.

From the diagrams shown in **Figure 8**, we can extract two kinds of information. Firstly, the most stable phase is the phase with the lowest free energy (ΔG), for a given $p\text{O}_2$ or applied potential. Secondly, we can infer whether or not a secondary oxide/peroxide bulk phase or monolayer can be formed by dopant segregation through Eq. 2. Since the dopant dissolved in the perovskite is the reference ($\Delta G = 0$), negative ΔG values in **Figure 8** for the oxide/peroxide bulk phases indicate that these phases are thermodynamically favored on LSM. This means that all the considered phases with $\Delta G(p\text{O}_2) < 0$ can be formed, even if they may not constitute the overall most stable phase. We therefore assume that in some cases segregated species can coexist, for instance, a monolayer and particles, as both may be thermodynamically favored over LSM.

From the intersections of the orange/green lines (oxide/peroxide phases, respectively) with the blue lines (dissolved dopant) in **Figure 8** we can infer the potential onset of dopant segregation under oxidizing conditions. This predicted onset condition can be compared with the experimentally determined transition (minimum of) enrichment of the dopant at the surface under anodic polarization as shown in **Figure 5**. In the case of LCM, the surface should become significantly enriched in Ca at potentials higher than +300 mV, where a CaO_2 monolayer is expected to form. Formation of CaO_2 particles may be observed in addition to a monolayer at potentials higher than +400 mV, where $\Delta G(\text{CaO}_{2,\text{bulk}})$ becomes negative. CaO as particle or

monolayer never constitutes the most stable compound, and is not expected to form under anodic polarization. The case of LSM is similar, but the onsets of SrO₂ monolayer and particle formation are shifted down to +270 and +380 mV, respectively. For LBM the situation is quite different due to the strongly negative wetting energy of BaO on the LBM (001) surface (cf. **Table 2**). For LBM, the most stable phase is a BaO monolayer at potentials between +80 mV and +220 mV. Above +220 mV the most stable phase is a BaO₂ monolayer. BaO₂ particles can appear on the surface above +200 mV.

In summary, the segregation onset shifts to less oxidizing conditions from Ca to Sr to Ba dopant cations in LaMnO₃. This can be rationalized on the basis of the trend in the chemical potentials of the dopant cations in the bulk of doped LaMnO₃, which increase by 0.83 eV from Ca to Sr to Ba (cf. **Table 1**), reflecting the increasing lattice strain due to increasing dopant cation radius. This increase in chemical potential along the series directly results in reduced solubility and increased tendency to precipitate.

5. Discussion

The reported observations on surface degradation in a lateral polarization gradient demonstrate both differences and similarities of the three compounds under scrutiny: In LCM, LSM, and LBM dopant cations segregate to the surface at high temperature (770°C) and form chemically different surface species. In highly reducing conditions (cathodic polarization) the extent of segregation increases⁵⁰ for all three compounds, whereas under oxidizing conditions (anodic polarization) an increase is observed only for LSM and LBM. The XPS results display dopant-specific trends of the extent of segregation as a function of bias voltage, showing a transition between the two regimes of segregation behavior for each compound. The different findings under oxidizing conditions for the three dopants were rationalized by theory, which shows a clear correlation between cation size, dopant chemical potential and segregation onset potential. In the following sections, we will review the key aspects and connect the observations made with the different techniques.

5.1. Different segregation mechanisms under anodic and cathodic polarization

We relate the polarization-dependent segregation behavior of the three different compounds to varying contributions of the two driving forces of segregation outlined in the introduction: an

elastic and an electrostatic force. Their balance in driving the segregation of the different dopants at different oxygen chemical potentials is subject of the two main hypotheses tested in the present report: 1) E_{elec} increases with a decrease in effective pO_2 and 2) E_{ela} increases with cation size mismatch, which shifts the onset of segregation to lower oxygen chemical potential with increasing cation size, as rationalized by theory.

The first hypothesis (E_{elec} increases with a decrease in effective pO_2) is dominant at negative potentials (cathodic polarization). For all three compounds, it was found that more negative potentials (corresponding to reducing conditions) increase segregation: -750 to +640 mV for LCM, -750 to +160 mV for LSM, and -750 to -160 mV for LBM. The *in-situ* APXPS data for cathodically polarized LSM in **Figures S2** and **S3** support the *ex-situ* observations reported here, and provide a reference for the local potential applied to the surface. The observed differences in the extent of segregation are even more pronounced owing to the high surface sensitivity of the synchrotron X-ray photoelectron spectroscopy at low kinetic energy (300 eV). Surface reduction creates oxygen vacancies, which attract the dopant to the surface electrostatically. Thus, the observed increase of segregation at decreasing effective oxygen pressures is in good agreement with hypothesis 1, predicting an increase of E_{elec} at reducing conditions.

The second hypothesis (E_{ela} increases with cation size mismatch) is dominant at positive potentials (anodic polarization), where bulk reactions between the dopant and the gas phase are enabled by the high oxygen chemical potentials. This leads to the formation of oxide and peroxide films at the surface. These reactions are favored for more reactive dopant cations, and the reactivity of a dopant in LaMnO_3 increases with cation size, as shown by our computations of the chemical potentials of dopants dissolved in LaMnO_3 . While the formation of dopant oxide precipitates itself is a consequence of the high oxygen chemical potential under anodic conditions, the onset potential of segregation shifts to lower oxygen chemical potentials with increasing cation size mismatch. This trend is reconciled between theory and experiment: experimentally, we observe that LBM has the lowest onset of segregation (**Figure 5**), while LCM has the highest onset potential of segregation under anodic polarization (**Figure S9**). Considering the formation of dopant oxide and peroxide phases, theory predicts the same trend based on the different dopant cation chemical potentials in the bulk of LCM, LSM, and LBM.

5.2. Observed trends for different dopants

Segregation in LCM was increased only with increasing cathodic polarization, but an increase with increasing anodic polarization was not observed. However, within the whole potential range, Ca is enriched at the surface compared to the as-prepared sample. In the cathodic polarization range, Ca exhibits a steep increase of the Ca_{surf} component in XPS with increasingly reducing conditions, as expected from the electrostatically driven dopant segregation. Even past the point of zero potential, the amount of segregated Ca appears to continue to decrease in our lateral polarization measurements up to +800 mV (**Figure 5**). This result is in apparent conflict with our computations that indicate that CaO_2 precipitation should be observed even in LCM at potentials higher than +400 mV. According to this theory, CaO_2 particle formation must be observed at some point in the anodic potential regime due to the μO_2 dependency of the precipitation free energy, even if the model has a large quantitative error. Thus, we tested this prediction in experiments under constant polarization at higher potentials (**Figure S9**) for LCM and LBM. The results of these measurements are consistent with the lateral polarization results in the area up to +640 mV where the data from the two setups overlaps. However, at +900 mV, we observe that the Ca content at the surface increases compared to that at +640 mV, possibly indicating the expected segregation onset. The discrepancy between experiment and calculation can be resolved employing a more detailed precipitation model that correctly captures the influence of defect concentrations on dopant precipitation, as shown shortly in **Section S5** and to be published elsewhere⁷⁸. Including the defect concentrations in the model shifts the precipitation onset for LCM to +807 mV. That is consistent with our experiments, where precipitation sets in between +640 mV and +900 mV. We clearly realize, supported by both theory and experiment, that LCM exhibits remarkable stability under anodic polarization. This can be explained by the fact that Ca is the smallest of the three dopants and exhibits barely any size mismatch with La. Since the contribution from the elastic energy is small for the Ca dopant in LCM, it has the lowest chemical potential in the (Ca, Sr, Ba) series, and thereby the lowest driving force for precipitation.

For LSM, quite in contrast, an increase of segregation under anodic polarization was found. This is because the higher elastic energy (as given by the higher chemical potential of Sr in LSM compared to Ca in LCM) shifts the segregation onset to a lower potential, which is qualitatively reproduced by theory. The larger cation mismatch between Sr and La significantly increases the impact of E_{ela} compared to Ca.

This behavior is found to be even more prominent in LBM owing to its larger cation radius. Due to the high misfit energy for Ba in LBM, the transition between electrostatically and elastically dominated segregation is shifted to -160 mV in the cathodic polarization range. This means that BaO/BaO₂ formation already occurs under reducing conditions. This strong shift is explained by theory, which shows that Ba in LBM has the highest chemical potential within the dopant series. The high elastic energy contribution for Ba results in a shift of the segregation onset potential to more reducing conditions.

These results show that the segregation onset potential under anodic polarization shifts to more reducing conditions with increasing cation radius. This agrees well with our initial expectations for dopants with different cation radii and the theoretical calculations that relate the cation radius with its chemical potential and, thereby, the onset of segregation. These observations support our second hypothesis of an elastic driving force that increases with dopant cation radius. Under cathodic polarization, on the other hand, an increase of segregation with more negative potential is observed for all three compounds in a similar way. This strongly supports the first hypothesis of an electrostatic driving force that is similar for all three dopants.

5.3. Surface chemistry and topography

In agreement with the spectroscopy results, measurements of the surface topography using SEM (**Figure 6**) and the roughness using AFM (**Figure S12**) display a gradual change across the surface of LCM, LSM, and LBM. In the case of LSM and LBM, a qualitative comparison of the amount of surface particles to the dopant core-level spectra, Sr 3*d* and Ba 4*d*, shows good agreement. A lot of particles are observed on the surface of LSM and LBM, under high cathodic and anodic bias, but less are found in between (cf. **Figure S11**). Particles in the positive potential region are smaller than those in the negative potential regime.

Overall, the increase of the dopant surface component in the series of XPS measurements as a function of the applied potential is strongly correlated with the coverage of particles on the surface in the cases of LSM and LBM. This is why we propose that the formation of a secondary dopant oxide phase explains the observed dopant enrichment at the surface. Only in the case of LCM, no particles are formed on the surface despite the increase of the Ca_{surf} signal in XPS under cathodic polarization. Instead the roughness measured by AFM increases under cathodic polarization (**Figure S12**), which appears to be related to the segregation.

5.4. Agreement between theory and experiment

Theory is applied to further elucidate the connection between cation size mismatch, oxygen chemical potential and dopant segregation. Our computations reflect the general trend of the elastic energy with cation size mismatch under oxidizing conditions. A larger cation size mismatch results in a larger chemical potential of the dopant cation, and results in reactions of the dopant with the gas phase oxygen under anodic polarization. Our computations show that the onset of segregation due to the formation of oxides and peroxides on the surface shifts to lower oxygen chemical potential with increasing dopant cation radius. The shift in segregation onset is caused by the elastic energy difference for different dopant cations. Experimentally, we observe (**Figure 5**) that for LCM, LSM, and LBM, the segregation onsets are beyond +800 mV (**Figure S9**), at +160 mV, and at -160 mV, respectively, i.e., the segregation onset shifts to lower potential within the alkaline earth series going to larger cation radii, from Ca to Ba. Our theoretical model predicts the onset of dopant enrichment in the form of a dopant peroxide (CaO_2 , SrO_2) or oxide (BaO) monolayer under anodic polarization at +300 mV, +270 mV, and +80 mV for LCM, LSM and LBM, respectively. Particle formation is expected on the surface for potentials greater than +400 mV, +380 mV, and +200 mV. Although the experimentally observed trend along the (Ca, Sr, Ba) series is qualitatively reproduced by the calculations, the segregation onset potential is not obtained quantitatively in the simple model presented here. As noted in **Section 5.2**, this discrepancy can mostly be resolved by treating precipitation in a defect model that equilibrates both the oxygen sublattice and the dopant with external reservoirs. However, as doped lanthanum manganites are quite complex, additional sources of uncertainty shown in more detail in **Section S4** in the supporting material.

We note that the present computations cover only the anodic polarization regime. Because the defect structure at the surface giving rise to the electrostatic driving force is more involved, we studied dopant surface segregation in detail only for the LSM (001) surface under cathodic polarization. These results will be published elsewhere ⁶⁵, but we provide a short summary of the results in **Section S6** in the supporting material. We make three observations relevant to the present manuscript: Near-surface Sr enrichment was shown to be favored under reducing conditions at all terminations that we considered (LaO , SrO , MnO_2 and several reconstructions). It is not driven by the intrinsic polarity of the surface, but rather by electrostatic attraction between the dopant and near-surface oxygen vacancies. Furthermore, the near-surface Sr content has a minimum (close to

+260 mV at 1050 K). While this minimum is located close to where it is found in our experiment on LSM (110) (+160 mV at 1050 K), this may be a coincidence because our model employs the (001) orientation rather than the (110) orientation. However, it is evident and encouraging also from the surface calculations that there is a minimum of the near-surface Sr content, and Sr enrichment can be observed under both anodic and cathodic polarization regime, consistent with our experiments.

6. Summary and Conclusion

The surface segregation of earth alkaline dopants (Ca, Sr, Ba) in doped lanthanum manganites under polarization has been investigated for a wide range of cathodic and anodic potentials by means of XPS, imaging techniques and DFT-based ab-initio thermodynamics. This combination of techniques allows for a systematic quantification (XPS), morphological surface characterization (SEM and AFM) and rationalization (theory) of the dopant segregation behavior as a function of effective oxygen pressures ranging from 10^{-16} to 10^{15} atm and of the dopant cation radius. We examine the two main origins of segregation proposed in the literature: the lattice mismatch of the dopant with the host cation La and the electrostatic attraction of the aliovalent dopants by a high oxygen vacancy density at the surface. The latter requires the presence of oxygen vacancies near the surface; we expect this contribution to dominate under reducing conditions. A higher misfit, on the other hand, has been shown by theory to increase the dopant chemical potential in the bulk, which enhances the precipitation of secondary compounds under oxidizing conditions. These responses to variations in the effective oxygen pressure are therefore expected to coexist, but dominate at opposite polarization regimes.

We examine the dopant segregation for three compounds with different dopant cation sizes ($\text{La}_{0.8}\text{Ca}_{0.2}\text{MnO}_3$, $\text{La}_{0.8}\text{Sr}_{0.2}\text{MnO}_3$, $\text{La}_{0.8}\text{Ba}_{0.2}\text{MnO}_3$) and indeed observe a U-shaped dependency of the amount of dopant segregation as a function of polarization by XPS for Sr and Ba. This result is confirmed by SEM surface imaging, which shows the highest coverage of particles on the surface at high cathodic and high anodic polarization and lower coverages in between. Only in the case of Ca, dopant enrichment at the surface and change of surface morphology was observed only in the cathodic polarization range. This is possibly due the fact that our measurement covers only the polarization range between -800 mV and +800 mV and the elastically dominated segregation may occur at even higher anodic polarization ($> +800$ mV). The minimum of the U-shaped curve

is interpreted as the transition point between the two driving forces (electrostatic under cathodic polarization and elastic under anodic polarization). The transition point shifts to higher oxygen chemical potential with increasing dopant cation radius ($R_{Ba} > R_{Sr} > R_{Ca}$). This behavior is rationalized by theory, which shows that the chemical potential of the dopant dissolved in lanthanum manganite increases with increasing cation radius. Since the precipitation of binary dopant oxide and peroxide phases is driven by reactions of the dopant with oxygen from the environment (while forming cation vacancies in the lanthanum manganite bulk), an increase of the dopant chemical potential will promote these reactions. The calculated precipitation onset shifts to lower potential with increasing dopant cation radius, which is qualitatively in agreement with the experimental observation. This allows us to conclude that under anodic polarization, segregation is indeed dominated by the elastic energy of the dopant.

We observe dopant segregation both under cathodic (low oxygen chemical potential) and under anodic (high oxygen chemical potential) conditions, and the relationship between dopant segregation and potential is non-monotonic. This observation provides a possible explanation for the fact that dopant segregation has been reported under many different conditions (both oxidizing and reducing) in literature, and resolves why a clear answer to whether reducing or oxidizing conditions are responsible for segregation has so far not been obtained. Our results show that segregation can occur under both oxidizing and reducing conditions in doped lanthanum manganites, which suggests that dopant segregation is a result of a nontrivial balance of electrostatic and elastic energies. Which one of these factors dominates depends on both the operating conditions and the size mismatch between dopant and host cations. Thus, the present study advances the mechanistic understanding of surface chemical degradation of perovskite-based energy conversion devices and has the potential to contribute to improving their long-term stability.

Acknowledgment

We thank the Air Force Office of Scientific Research (Grant No: FA9550-16-1-0427) for supporting this research. Dongha Kim thanks the Kwanjeong Educational Foundation for a partial graduate student fellowship. Roland Bliem acknowledges support from the Austrian Science Fund (FWF) in the form of an Erwin Schrödinger Fellowship (project J 4099-N34). Franziska Hess acknowledges the Deutsche Forschungsgemeinschaft for a postdoc fellowship. This work made

use of the Shared Experimental Facilities supported in part by the MRSEC Program of the National Science Foundation under award number DMR-1419807. Computational time was provided by XSEDE and NERSC on the Stampede2 and Cori high performance computing clusters. We gratefully acknowledge the staff at TACC, NERSC and MGHPCC for technical support. Also, we acknowledge support from Sunho Kim for SEM measurements and support from Gülin Vardar and William Bowman for synchrotron measurements. AP-XPS measurements were done on the end station of Sorbonne Université set at the TEMPO beamline at SOLEIL and were performed as part of proposal 20161121. We thank Fabrice Bournel for helping the measurement.

Supporting material

Section S1: Sources of contamination

Section S2: AP-XPS measurements and supplementary experimental data

Section S3: Formation energies of (Ca, Sr, Ba) oxides and peroxides

Section S4: Detailed analysis of computational uncertainty

Section S5: Preliminary results on dopant precipitation in a defect chemistry model

Section S6: Dopant enrichment at the LSM (001) surface

Section S7: Effective oxygen chemical potential of LDM thin films

Section S8: Errors associated with fitting the X-ray photoelectron spectra

Section S9: Negligible effect of joule heating of LDM thin film on its temperature

Section S10: Calculation of the inelastic mean free path of each core-level electron

Figure S1: Comparison between as-deposited and etched samples

Figure S2: La 4d spectra at 650°C

Figure S3: Sr 3d spectra at 650°C

Figure S4: Thickness of LDM films measured using a Bruker DXT Stylus Profilometer

Figure S5: SEM images of as-prepared samples

Figure S6: XRD spectra after annealing at 770°C

Figure S7: La 4d and Mn 3p XPS spectra

Figure S8: Ratios of $D/(La+D)$, $D_{latt}/(La+D)$, D/Mn , and D_{latt}/Mn at different potentials

Figure S9: Additional polarization results for LCM and LBM

Figure S10: XRD pattern of LBM and LCM samples used for separate polarization experiment

Figure S11: area coverages of surface particles on LSM and LBM

Figure S12: AFM images surface roughness

Figure S13: Total energy of strained SrO₂ with respect to the lattice c vector

Figure S14: Structures of SrO₂ stretched to fit the LSM lattice

Figure S15: Phase precipitation in LDM

Figure S16: Near-surface Sr content computed for anodic and cathodic polarization

Figure S17: Errors associated with fitting XPS spectra

Figure S18: Brief configuration of our experimental setup

Figure S19: Temperature change of LDM thin film during thermal balance

Table S1: Formation energies of dopant oxides and peroxides from DFT and experiment

Table S2: Dopant chemical potentials estimated for oxidized and reduced LDMs

Table S3: Experimental values used for plotting temperature vs. time graph in Figure S19

Table S4: Experimental values used for calculating heat transfer coefficient, h

Table S5: IMFP values of the chosen core-level photoelectrons from LBM, LSM, and LCM

References

1. Singhal, S. C., Advances in solid oxide fuel cell technology. *Solid State Ionics* **2000**, *135* (1–4), 305-313.
2. Singhal, S. C.; Kendall, K., *High-temperature solid oxide fuel cells: fundamentals, design and applications*. Elsevier: 2003.
3. Gorte, R. J.; Vohs, J. M., Catalysis in Solid Oxide Fuel Cells. *Annual Review of Chemical and Biomolecular Engineering* **2011**, *2* (1), 9-30.
4. Kuklja, M. M.; Kotomin, E. A.; Merkle, R.; Mastrikov, Y. A.; Maier, J., Combined theoretical and experimental analysis of processes determining cathode performance in solid oxide fuel cells. *Physical Chemistry Chemical Physics* **2013**, *15* (15), 5443-5471.
5. Laguna-Bercero, M. A., Recent advances in high temperature electrolysis using solid oxide fuel cells: A review. *Journal of Power Sources* **2012**, *203*, 4-16.
6. Kilner, J. A.; Burriel, M., Materials for intermediate-temperature solid-oxide fuel cells. *Annual Review of Materials Research* **2014**, *44*, 365-393.
7. Shin, T. H.; Ida, S.; Ishihara, T., Doped CeO₂-LaFeO₃ composite oxide as an active anode for direct hydrocarbon-type solid oxide fuel cells. *Journal of the American Chemical Society* **2011**, *133* (48), 19399-407.
8. Habib, M. A.; Nemitallah, M.; Ben-Mansour, R., Recent Development in Oxy-Combustion Technology and Its Applications to Gas Turbine Combustors and ITM Reactors. *Energy & Fuels* **2013**, *27* (1), 2-19.
9. Adler, S. B.; Lane, J. A.; Steele, B. C. H., Electrode Kinetics of Porous Mixed-Conducting Oxygen Electrodes. *Journal of The Electrochemical Society* **1996**, *143* (11), 3554-3564.
10. Kim, J.; Yin, X.; Tsao, K. C.; Fang, S.; Yang, H., Ca₂Mn₂O₅ as oxygen-deficient perovskite electrocatalyst for oxygen evolution reaction. *Journal of the American Chemical Society* **2014**, *136* (42), 14646-9.
11. Kim, B. J.; Fabbri, E.; Abbott, D. F.; Cheng, X.; Clark, A. H.; Nachtegaal, M.; Borlaf, M.; Castelli, I. E.; Graule, T.; Schmidt, T. J., Functional Role of Fe-Doping in Co-Based Perovskite Oxide Catalysts for Oxygen Evolution Reaction. *Journal of the American Chemical Society* **2019**, *141* (13), 5231-5240.

12. Risch, M.; Stoerzinger, K. A.; Maruyama, S.; Hong, W. T.; Takeuchi, I.; Shao-Horn, Y., La(0.8)Sr(0.2)MnO(3-delta) decorated with Ba_{0.5}Sr_{0.5}Co_{0.8}Fe_{0.2}O_{3-δ}: a bifunctional surface for oxygen electrocatalysis with enhanced stability and activity. *Journal of the American Chemical Society* **2014**, *136* (14), 5229-32.
13. Hamada, I.; Uozumi, A.; Morikawa, Y.; Yanase, A.; Katayama-Yoshida, H., A density functional theory study of self-regenerating catalysts LaFe_{1-x}M_xO_{3-y} (M = Pd, Rh, Pt). *Journal of the American Chemical Society* **2011**, *133* (46), 18506-9.
14. Jo, Y. R.; Koo, B.; Seo, M. J.; Kim, J. K.; Lee, S.; Kim, K.; Han, J. W.; Jung, W.; Kim, B. J., Growth Kinetics of Individual Co Particles Ex-solved on SrTi_{0.75}Co_{0.25}O_{3-δ} Polycrystalline Perovskite Thin Films. *Journal of the American Chemical Society* **2019**, *141* (16), 6690-6697.
15. Hauch, A.; Jensen, S. H.; Ramousse, S.; Mogensen, M., Performance and durability of solid oxide electrolysis cells. *Journal of The Electrochemical Society* **2006**, *153* (9), A1741-A1747.
16. Waser, R.; Aono, M., Nanoionics-based resistive switching memories. *Nature Materials* **2007**, *6* (11), 833-840.
17. Garcia-Martin, S.; Alario-Franco, M. A.; Ehrenberg, H.; Rodriguez-Carvajal, J.; Amador, U., Crystal structure and microstructure of some La_{2/3-x}Li_{3x}TiO₃ oxides: an example of the complementary use of electron diffraction and microscopy and synchrotron X-ray diffraction to study complex materials. *Journal of the American Chemical Society* **2004**, *126* (11), 3587-96.
18. Takeguchi, T.; Yamanaka, T.; Takahashi, H.; Watanabe, H.; Kuroki, T.; Nakanishi, H.; Orikasa, Y.; Uchimoto, Y.; Takano, H.; Ohguri, N.; Matsuda, M.; Murota, T.; Uosaki, K.; Ueda, W., Layered perovskite oxide: a reversible air electrode for oxygen evolution/reduction in rechargeable metal-air batteries. *Journal of the American Chemical Society* **2013**, *135* (30), 11125-30.
19. Kilner, J.; Berenov, A.; Rossiny, J., Diffusivity of the Oxide ion in Perovskite Oxides. In *Perovskite Oxide for Solid Oxide Fuel Cells*, Springer: 2009; pp 95-116.
20. Mastrikov, Y. A.; Merkle, R.; Heifets, E.; Kotomin, E. A.; Maier, J., Pathways for Oxygen Incorporation in Mixed Conducting Perovskites: A DFT-Based Mechanistic Analysis for (La, Sr)MnO_{3-δ}. *The Journal of Physical Chemistry C* **2010**, *114* (7), 3017-3027.
21. Fleig, J.; Kim, H. R.; Jamnik, J.; Maier, J., Oxygen Reduction Kinetics of Lanthanum Manganite (LSM) Model Cathodes: Partial Pressure Dependence and Rate-Limiting Steps. *Fuel Cells* **2008**, *8* (5), 330-337.
22. Hess, F.; Staykov, A. T.; Yildiz, B.; Kilner, J., Solid Oxide Fuel Cell Materials and Interfaces. In *Handbook of Materials Modeling. Volume 2 Applications: Current and Emerging Materials*, Andreoni, W.; Yip, S., Eds. Springer, Cham: 2018.
23. Akbay, T.; Staykov, A.; Druce, J.; Téllez, H.; Ishihara, T.; Kilner, J. A., The interaction of molecular oxygen on LaO terminated surfaces of La₂NiO₄. *J. Mater. Chem. A* **2016**, *4*, 13113-13124.
24. Staykov, A.; Téllez, H.; Akbay, T.; Druce, J.; Ishihara, T.; Kilner, J., Oxygen Activation and Dissociation on Transition Metal Free Perovskite Surfaces. *Chem. Mater.* **2015**, *27*, 8273-8281.
25. A.Banerjee; O.Deutschmann, Elementary kinetics of the oxygen reduction reaction on LSM-YSZ composite cathodes. *J. Catal.* **2017**, *346*, 30-49.
26. Adler, S. B., Factors Governing Oxygen Reduction in Solid Oxide Fuel Cell Cathodes. *Chemical Reviews* **2004**, *104* (10), 4791-4844.
27. Singhal, S. C., Solid Oxide Fuel Cells: Status, Challenges and Opportunities. *Advances in Science and Technology* **2006**, *45*, 1837-1846.
28. Cai, Z.; Kubicek, M.; Fleig, J.; Yildiz, B., Chemical Heterogeneities on La_{0.6}Sr_{0.4}CoO_{3-δ} Thin Films—Correlations to Cathode Surface Activity and Stability. *Chemistry of Materials* **2012**, *24* (6), 1116-1127.

29. Kubicek, M.; Limbeck, A.; Frömling, T.; Hutter, H.; Fleig, J., Relationship between Cation Segregation and the Electrochemical Oxygen Reduction Kinetics of $\text{La}_{0.6}\text{Sr}_{0.4}\text{CoO}_{3-\delta}$ Thin Film Electrodes. *Journal of The Electrochemical Society* **2011**, *158* (6), B727-B734.
30. Druce, J.; Tellez, H.; Burriel, M.; Sharp, M. D.; Fawcett, L. J.; Cook, S. N.; McPhail, D. S.; Ishihara, T.; Brongersma, H. H.; Kilner, J. A., Surface termination and subsurface restructuring of perovskite-based solid oxide electrode materials. *Energy & Environmental Science* **2014**, *7* (11), 3593-3599.
31. Rupp, G. M.; Limbeck, A.; Kubicek, M.; Penn, A.; Stoger-Pollach, M.; Friedbacher, G.; Fleig, J., Correlating surface cation composition and thin film microstructure with the electrochemical performance of lanthanum strontium cobaltite (LSC) electrodes. *Journal of Materials Chemistry A* **2014**, *2* (19), 7099-7108.
32. Porotnikova, N. M.; Eremin, V. A.; Farlenkov, A. S.; Kurumchin, E. K.; Sherstobitova, E. A.; Kochubey, D. I.; Ananyev, M. V., Effect of AO Segregation on Catalytical Activity of $\text{La}_{0.7}\text{A}_{0.3}\text{MnO}_{3\pm\delta}$ (A = Ca, Sr, Ba) Regarding Oxygen Reduction Reaction. *Catalysis Letters* **2018**, *148*, 2839-2847.
33. Lee, W.; Han, J. W.; Chen, Y.; Cai, Z.; Yildiz, B., Cation size mismatch and charge interactions drive dopant segregation at the surfaces of manganite perovskites. *Journal of the American Chemical Society* **2013**, *135* (21), 7909-25.
34. Poulsen, F. W., Defect chemistry modelling of oxygen-stoichiometry, vacancy concentrations, and conductivity of $(\text{La}_{1-x}\text{Sr}_x)_y\text{MnO}_{3\pm\delta}$. *Solid State Ionics* **2000**, *129* (1), 145-162.
35. Konyshova, E. Y.; Xu, X.; Irvine, J. T., On the existence of A-site deficiency in perovskites and its relation to the electrochemical performance. *Advanced Materials* **2012**, *24* (4), 528-32.
36. Tsvetkov, N.; Lu, Q.; Sun, L.; Crumlin, E. J.; Yildiz, B., Improved chemical and electrochemical stability of perovskite oxides with less reducible cations at the surface. *Nature Materials* **2016**, *15* (9), 1010-6.
37. Niania, M.; Podor, R.; Britton, T. B.; Li, C.; Cooper, S. J.; Svetkov, N.; Skinner, S.; Kilner, J., In situ study of strontium segregation in $\text{La}_{0.6}\text{Sr}_{0.4}\text{Co}_{0.2}\text{Fe}_{0.8}\text{O}_{3-\delta}$ in ambient atmospheres using high-temperature environmental scanning electron microscopy. *Journal of Materials Chemistry A* **2018**, *6* (29), 14120-14135.
38. Kubicek, M.; Rupp, G. M.; Huber, S.; Penn, A.; Opitz, A. K.; Bernardi, J.; Stoger-Pollach, M.; Hutter, H.; Fleig, J., Cation diffusion in $\text{La}_{0.6}\text{Sr}_{0.4}\text{CoO}_{3-\delta}$ below 800 degrees C and its relevance for Sr segregation. *Phys Chem Chem Phys* **2014**, *16* (6), 2715-26.
39. Pişkin, F.; Bliem, R.; Yildiz, B., Effect of crystal orientation on the segregation of aliovalent dopants at the surface of $\text{La}_{0.6}\text{Sr}_{0.4}\text{CoO}_3$. *Journal of Materials Chemistry A* **2018**, *6* (29), 14136-14145.
40. Zuev, A. Y.; Tsvetkov, D. S., Oxygen nonstoichiometry, defect structure and defect-induced expansion of undoped perovskite $\text{LaMnO}_{3\pm\delta}$. *Solid State Ionics* **2010**, *181* (11), 557-563.
41. Saiful Islam, M., Ionic transport in ABO_3 perovskite oxides: a computer modelling tour. *Journal of Materials Chemistry* **2000**, *10* (4), 1027-1038.
42. Katsiev, K.; Yildiz, B.; Balasubramaniam, K.; Salvador, P. A., Electron tunneling characteristics on $\text{La}_{0.7}\text{Sr}_{0.3}\text{MnO}_3$ thin-film surfaces at high temperature. *Applied Physics Letters* **2009**, *95* (9), 092106.
43. Fister, T. T.; Fong, D. D.; Eastman, J. A.; Baldo, P. M.; Highland, M. J.; Fuoss, P. H.; Balasubramaniam, K. R.; Meador, J. C.; Salvador, P. A., In situ characterization of strontium surface segregation in epitaxial $\text{La}_{0.7}\text{Sr}_{0.3}\text{MnO}_3$ thin films as a function of oxygen partial pressure. *Applied Physics Letters* **2008**, *93* (15), 151904-151904.
44. Crumlin, E. J.; Mutoro, E.; Hong, W. T.; Biegalski, M. D.; Christen, H. M.; Liu, Z.; Bluhm, H.; Shao-Horn, Y., In Situ Ambient Pressure X-ray Photoelectron Spectroscopy of Cobalt Perovskite Surfaces under Cathodic Polarization at High Temperatures. *The Journal of Physical Chemistry C* **2013**, *117* (31), 16087-16094.

45. Mutoro, E.; Crumlin, E. J.; Pöpke, H.; Luerssen, B.; Amati, M.; Abyaneh, M. K.; Biegalski, M. D.; Christen, H. M.; Gregoratti, L.; Janek, J.; Shao-Horn, Y., Reversible Compositional Control of Oxide Surfaces by Electrochemical Potentials. *The Journal of Physical Chemistry Letters* **2012**, 3 (1), 40-44.
46. Baumann, F. S.; Fleig, J.; Konuma, M.; Starke, U.; Habermeier, H.-U.; Maier, J., Strong Performance Improvement of $\text{La}_{0.6}\text{Sr}_{0.4}\text{Co}_{0.8}\text{Fe}_{0.2}\text{O}_{3-\delta}$ SOFC Cathodes by Electrochemical Activation. *Journal of The Electrochemical Society* **2005**, 152 (10), A2074-A2079.
47. Ullmann, H.; Trofimenko, N.; Tietz, F.; Stöver, D.; Ahmad-Khanlou, A., Correlation between thermal expansion and oxide ion transport in mixed conducting perovskite-type oxides for SOFC cathodes. *Solid State Ionics* **2000**, 138 (1-2), 79-90.
48. Opitz, A. K.; Kubicek, M.; Huber, S.; Huber, T.; Holzlechner, G.; Hutter, H.; Fleig, J., Thin film cathodes in SOFC research: How to identify oxygen reduction pathways? *Journal of Materials Research* **2013**, 28 (16), 2085-2105.
49. la O', G. J.; Savinell, R. F.; Shao-Horn, Y., Activity Enhancement of Dense Strontium-Doped Lanthanum Manganite Thin Films under Cathodic Polarization: A Combined AES and XPS Study. *Journal of The Electrochemical Society* **2009**, 156 (6), B771.
50. Huber, A.-K.; Falk, M.; Rohnke, M.; Luerssen, B.; Amati, M.; Gregoratti, L.; Hesse, D.; Janek, J., In situ study of activation and de-activation of LSM fuel cell cathodes – Electrochemistry and surface analysis of thin-film electrodes. *Journal of Catalysis* **2012**, 294, 79-88.
51. Huber, A. K.; Falk, M.; Rohnke, M.; Luerssen, B.; Gregoratti, L.; Amati, M.; Janek, J., In situ study of electrochemical activation and surface segregation of the SOFC electrode material $\text{La}_{0.75}\text{Sr}_{0.25}\text{Cr}_{0.5}\text{Mn}_{0.5}\text{O}_{3\pm\delta}$. *Phys Chem Chem Phys* **2012**, 14 (2), 751-8.
52. Caillol, N.; Pijolat, M.; Siebert, E., Investigation of chemisorbed oxygen, surface segregation and effect of post-treatments on $\text{La}_{0.8}\text{Sr}_{0.2}\text{MnO}_3$ powder and screen-printed layers for solid oxide fuel cell cathodes. *Applied Surface Science* **2007**, 253 (10), 4641-4648.
53. Wang, W.; Jiang, S., A mechanistic study on the activation process of (La, Sr) MnO_3 electrodes of solid oxide fuel cells. *Solid State Ionics* **2006**, 177 (15-16), 1361-1369.
54. Jiang, S. P.; Love, J. G., Origin of the initial polarization behavior of Sr-doped LaMnO_3 for O_2 reduction in solid oxide fuel cells. *Solid State Ionics* **2001**, 138 (3), 183-190.
55. Wang, F.; Nishi, M.; Brito, M. E.; Kishimoto, H.; Yamaji, K.; Yokokawa, H.; Horita, T., Sr and Zr diffusion in LSCF/10GDC/8YSZ triplets for solid oxide fuel cells (SOFCs). *Journal of Power Sources* **2014**, 258, 281-289.
56. Laurencin, J.; Hubert, M.; Sanchez, D. F.; Pylypko, S.; Morales, M.; Morata, A.; Morel, B.; Montinaro, D.; Lefebvre-Joud, F.; Siebert, E., Degradation mechanism of $\text{La}_{0.6}\text{Sr}_{0.4}\text{Co}_{0.2}\text{Fe}_{0.8}\text{O}_{3-\delta}/\text{Gd}_{0.1}\text{Ce}_{0.9}\text{O}_{2-\delta}$ composite electrode operated under solid oxide electrolysis and fuel cell conditions. *Electrochimica Acta* **2017**, 241, 459-476.
57. Huber, T. M.; Navickas, E.; Sasaki, K.; Yildiz, B.; Tuller, H.; Friedbacher, G.; Hutter, H.; Fleig, J., Experimental Design for Voltage Driven Tracer Incorporation and Diffusion Studies on Oxide Thin Film Electrodes. *Journal of The Electrochemical Society* **2017**, 164 (7), F809-F814.
58. Lee, Y.-L.; Morgan, D., Prediction of Surface Oxygen Vacancy Concentrations of $(\text{La}_{1-x}\text{Sr}_x)\text{MnO}_3$. *ECS Transactions* **2009**, 25 (2), 2769-2774.
59. Lee, Y.-L.; Kleis, J.; Rossmeisl, J.; Morgan, D., *Ab initio* energetics of LaBO_3 (001) (B = Mn, Fe, Co, and Ni) for solid oxide fuel cell cathodes. *Physical Review B* **2009**, 80 (22), 224101.
60. Carrasco, J.; Illas, F.; Lopez, N.; Kotomin, E. A.; Zhukovskii, Y. F.; Evarestov, R. A.; Mastrokov, Y. A.; Piskunov, S.; Maier, J., First-principles calculations of the atomic and electronic structure of F centers in the bulk and on the (001) surface of SrTiO_3 . *Physical Review B* **2006**, 73 (6), 064106.
61. Bishop, S. R.; Duncan, K. L.; Wachsman, E. D., Surface and bulk oxygen non-stoichiometry and bulk chemical expansion in gadolinium-doped cerium oxide. *Acta Materialia* **2009**, 57 (12), 3596-3605.
62. Mullins, D. R., The surface chemistry of cerium oxide. *Surface Science Reports* **2015**, 70 (1), 42-85.

63. Bjørheim, T. S.; Kuwabara, A.; Mohn, C. E.; Norby, T., Defects at the (110) surface of rutile TiO₂ from ab initio calculations. *International Journal of Hydrogen Energy* **2012**, 37 (9), 8110-8117.
64. Tompsett, D. A.; Parker, S. C.; Islam, M. S., Rutile (β-)MnO₂ Surfaces and Vacancy Formation for High Electrochemical and Catalytic Performance. *Journal of the American Chemical Society* **2014**, 136 (4), 1418-1426.
65. Hess, F.; Yildiz, B., accepted in *Phys. Rev. Mater.* **2019**.
66. Lee, W.; Han, J. W.; Chen, Y.; Cai, Z.; Yildiz, B., Cation Size Mismatch and Charge Interactions Drive Dopant Segregation at the Surfaces of Manganite Perovskites. *J. Am. Chem. Soc.* **2013**, 135, 7909-7925.
67. Lee, W.; Yildiz, B., Factors that Influence Cation Segregation at the Surfaces of Perovskite Oxides. *ECS Transactions* **2013**, 57 (1), 2115-2123.
68. Druce, J.; Tellez, H.; Burriel, M.; Sharp, M. D.; Fawcett, L. J.; Cook, S. N.; McPhail, D. S.; Ishihara, T.; Brongersma, H. H.; Kilner, J. A., Surface termination and subsurface restructuring of perovskite-based solid oxide electrode materials. *Energy Environ. Sci.* **2014**, 7, 3539–3599.
69. Bertacco, R.; Contour, J. P.; Barthélemy, A.; Olivier, J., Evidence for strontium segregation in La_{0.7}Sr_{0.3}MnO₃ thin films grown by pulsed laser deposition: consequences for tunnelling junctions. *Surf. Sci.* **2002**, 511, 366-372.
70. NIST Database 71; U.S. Department of Commerce: Washington, DC, 2001, accessed in 2017/2018.
71. Values acquired from the KolXPD spectrum fitting program.
72. Kresse, G.; Furthmüller, J., Efficient iterative schemes for ab initio total-energy calculations using a plane-wave basis set. *Phys. Rev. B* **1996**, 54, 11169-11186.
73. Perdew, J. P.; Chevary, J. A.; Vosko, S. H.; Jackson, K. A.; Pederson, M. R.; Singh, D. J.; Fiolhais, C., Atoms, molecules, solids, and surfaces: Applications of the generalized gradient approximation for exchange and correlation. *Phys. Rev. B* **1992**, 46, 6671-6687.
74. Dudarev, S. L.; Botton, G. A.; Savrasov, S. Y.; Humphreys, C. J.; Sutton, A. P., Electron-energy-loss spectra and the structural stability of nickel oxide: An LSDA+U study. *Phys. Rev. B* **1998**, 57, 1505-1509.
75. Wang, L.; Maxisch, T.; Ceder, G., Oxidation energies of transition metal oxides within the GGA+U framework. *Phys. Rev. B* **2006**, 73, 195107-195107.
76. NIST Chemistry webbook.
77. Chen, Y.; Téllez, H.; Burriel, M.; Yang, F.; Tsvetkov, N.; Cai, Z.; McComb, D. W.; Kilner, J. A.; Yildiz, B., Segregated Chemistry and Structure on (001) and (100) Surfaces of (La_{1-x}Sr_x)₂CoO₄ Override the Crystal Anisotropy in Oxygen Exchange Kinetics. *Chemistry of Materials* **2015**, 27 (15), 5436-5450.
78. Hess, F.; Yildiz, B., *In preparation* **2019**.

